

Search for the lepton-family-number nonconserving decay $\mu^+ \rightarrow e^+ \gamma$

M. Ahmed,^{3,a} J. F. Amann,⁵ D. Barlow,^{8,b} K. Black,^{5,c} R. D. Bolton,⁵ M. L. Brooks,⁵ S. Carius,^{5,d} Y. K. Chen,^{3,e} A. Chernyshev,⁵ H. M. Concannon,⁹ M. D. Cooper,⁵ P. S. Cooper,² J. Crocker,^{1,f} J. R. Dittmann,^{9,g} M. Dzemidzic,^{3,h} A. Empl,³ R. J. Fisk,⁹ E. Fleet,^{11,i} W. Foreman,⁵ C. A. Gagliardi,⁷ D. Haim,^{11,j} A. Hallin,^{5,k} C. M. Hoffman,⁵ G. E. Hogan,⁵ E. B. Hughes,^{6,l} E. V. Hungerford III,³ C. C. H. Jui,^{6,m} G. J. Kim,⁷ J. E. Knott,⁴ D. D. Koetke,⁹ T. Kozlowski,⁵ M. A. Kroupa,^{5,n} A. R. Kunselman,¹² K. A. Lan,³ V. Laptev,⁵ D. Lee,⁵ F. Liu,^{7,o} R. W. Manweiler,⁹ R. Marshall,¹⁰ B. W. Mayes II,³ R. E. Mischke,⁵ B. M. K. Nefkens,⁸ L. M. Nickerson,^{9,p} P. M. Nord,⁹ M. A. Othoudt,⁵ J. N. Otis,^{6,q} R. Phelps,^{3,r} L. E. Piilonen,¹¹ C. Pillai,^{5,8} L. Pinsky,³ M. W. Ritter,^{6,s} C. Smith,^{11,t} T. D. S. Stanislaus,^{5,9} K. M. Stantz,^{4,u} J. J. Szymanski,⁵ L. Tang,^{3,v} W. B. Tippens,^{10,8,w} R. E. Tribble,⁷ X. L. Tu,^{7,x} L. A. Van Ausdeln,^{7,y} W. H. von Witch,^{3,z} D. Whitehouse,^{5,aa} C. Wilkinson,⁵ B. Wright,¹⁰ S. C. Wright,¹ Y. Zhang,^{11,bb} and K. O. H. Ziock^{10,cc}

(MEGA Collaboration)

¹University of Chicago, Chicago, Illinois 60637²Fermi National Accelerator Laboratory, Batavia, Illinois 60510³University of Houston, Houston, Texas 77204⁴Indiana University, Bloomington, Indiana 46383⁵Los Alamos National Laboratory, Los Alamos, New Mexico 87545⁶Stanford University, Stanford, California 94305⁷Texas A & M University, College Station, Texas 77843⁸University of California Los Angeles, Los Angeles, California 90095⁹Valparaiso University, Valparaiso, Indiana 46383¹⁰University of Virginia, Charlottesville, Virginia 22901¹¹Virginia Polytechnic Institute and State University, Blacksburg, Virginia 24061¹²University of Wyoming, Laramie, Wyoming 82071

(Received 6 November 2001; published 7 June 2002)

The MEGA experiment, which searched for the muon- and electron-number violating decay $\mu^+ \rightarrow e^+ \gamma$, is described. The spectrometer system, the calibrations, the data taking procedures, the data analysis, and the sensitivity of the experiment are discussed. The most stringent upper limit on the branching ratio, $\mathcal{B}(\mu^+ \rightarrow e^+ \gamma) < 1.2 \times 10^{-11}$ with 90% confidence, is derived from a likelihood analysis.

DOI: 10.1103/PhysRevD.65.112002

PACS number(s): 13.35.Bv, 11.30.Fs, 11.30.Hv, 13.10.+q

^aPermanent address: Duke University, Durham, NC 27708.^bPermanent address: Washington State University, Pullman, WA 99164.^cPermanent address: Goddard Space Flight Center, Greenbelt, MD 20740.^dPermanent address: Uppsala University, 751 05 Uppsala, Sweden.^ePermanent address: Zhejiang Silk and Textile University, Hangzhou, China 310012.^fPermanent address: Caltech/Applied Physics, Pasadena, CA 91125.^gPermanent address: Fermilab, Batavia, IL 60510.^hPermanent address: Indiana University School of Medicine, Indianapolis, IN 46202.ⁱPermanent address: University of Maryland, College Park, MD 21201.^jPermanent address: InSystems Technologies, Roanoke VA 240110.^kPermanent address: Queens University, Kingston, Ontario, Canada K7L 3N6.^lDeceased.^mPermanent address: University of Utah, Salt Lake City, UT 84112.ⁿPermanent address: Monmouth College, Monmouth, IL 61462.^oPermanent address: Vina Technologies, Newark, CA 94560.^pPermanent address: Illinois Mathematics and Science Academy, Aurora, IL 60506.^qPermanent address: IBM Corp., Austin, TX 78758.^rPermanent address: IBM Microelectronics Division, Essex Junction, VT 05452.^sPermanent address: Salinas, CA 93901.^tPermanent address: Johns Hopkins University, Baltimore, MD 21218.^uPermanent address: Optosonics, Inc., Indianapolis, IN 46260.^vPermanent address: Hampton University, Hampton, VA 23668.^wPermanent address: US Department of Energy, Germantown, MD 20874.^xPermanent address: Cisco Systems, Inc., Richardson, TX 75082.^yPermanent address: Idaho National Engineering and Environmental Laboratory, Idaho Falls, ID 83401.^zPermanent address: University of Bonn, Bonn, West Germany.^{aa}Permanent address: Allied Group, Glastonbury, CT 06033.^{bb}Permanent address: AT&T Labs, Middletown, NJ 07932.^{cc}Permanent address: Albuquerque, NM 87123.

I. INTRODUCTION

The standard $SU(3)\times SU(2)\times U(1)$ model of the strong and electroweak interactions has proved to be remarkably successful in describing current experimental results, with only the evidence for neutrino oscillations [1] and the recent measurement of the muon anomalous magnetic moment [2] falling outside its expectations. The standard model is nonetheless believed to be an effective low-energy approximation of a more fundamental theory as it contains many free parameters and unexplained symmetries. Many extensions to the standard model have been proposed. Often these are motivated by attempts to justify features, like parity violation or lepton-family-number conservation, which are put in “by hand” to explain experimental data.

Essentially every extension of the standard model includes new heavy particles that mediate rare decays that are otherwise forbidden. The most sensitive decay mode varies by model, so it is important to study a range of rare decays in the search for new physics. The rare decay $\mu\rightarrow e\gamma$ is the classic example of a reaction that would be allowed except for the separate conservation of muon and electron numbers within the standard model; in fact, $\mu\rightarrow e\gamma$ is predicted to occur in most proposed extensions. For example, it has been shown that a broad range of grand unified supersymmetric theories predict that $\mu\rightarrow e\gamma$ should occur with a branching ratio in the range 10^{-10} – 10^{-14} [3], and the current world limits on $\mu\rightarrow e\gamma$ and other lepton-family-number violating decays — including $\mu\rightarrow e\gamma\gamma$, $\mu\rightarrow eee$ and $\mu\rightarrow e$ conversion in a muonic atom — have been used to set limits on many proposed extensions to the standard model. Reference [4] provides a recent review.

The MEGA Collaboration was formed to search for the decay $\mu\rightarrow e\gamma$ at the Los Alamos Meson Physics Facility (LAMPF). The most sensitive previous limit, $\mathcal{B}(\mu^+\rightarrow e^+\gamma) < 4.9\times 10^{-11}$ (90% C.L.), was obtained with the Crystal Box detector [5]. The MEGA experiment produced a new upper limit on the branching ratio, $\mathcal{B}(\mu^+\rightarrow e^+\gamma) < 1.2\times 10^{-11}$ (90% C.L.), as discussed briefly in Ref. [6]. This paper presents a more complete description of the experiment and its results.

II. EXPERIMENTAL DESIGN PHILOSOPHY

The MEGA experiment was designed to find the decay $\mu^+\rightarrow e^+\gamma$ in a background-free environment if its branching ratio was greater than 10^{-13} . The decay was to be isolated from all backgrounds by its unique kinematic signature: a muon at rest decaying into a time and spatially coincident photon and positron with equal and opposite momenta of 52.8 MeV/ c . The identification of the $\mu\rightarrow e\gamma$ signal relied on precise and accurate measurements of the vector momenta of the photon and the positron at the muon decay point and their relative times.

Accordingly, a high precision magnetic spectrometer system was constructed with two distinct and separated parts: (a) a low-mass system of multiple-wire proportional chambers (MWPCs) to track the positron orbits plus a series of plastic scintillators to determine the end time of the positron

orbit and (b) pair spectrometers to detect the photons and determine their energy, propagation direction, conversion time and location. To extract the vector momentum of the photon, the intersection of the positron with the target was assumed to be the origin of the photon. The replacement of the total absorption calorimeter used in previous experiments by pair spectrometers was a trade-off of detection efficiency for resolution, solid angle, and temporal stability. To maximize the solid angle acceptance, the photon system nearly surrounded the positron detection system. The magnetic field was produced by a superconducting solenoid, and the spectrometer system was cylindrical in shape, with the cylinder axis parallel to the solenoid field.

The positron MWPCs were constructed with as little mass as possible to minimize dE/dx energy loss, annihilation in flight, and multiple scattering. Otherwise the positron energy and position resolutions would be degraded and the photon backgrounds would be worse. This requirement implied that no support structures for the MWPCs could be located in the positron orbit region. The positron spectrometer was segmented in a way that minimized the occupancy in a high rate environment, especially in the presence of magnetically trapped positrons. The muon decay target had to have sufficient mass to stop the muon, but conversely had to impose minimum mass through which the positron would pass, which dictated a passive target. These conditions were met by a target that was highly inclined with respect to the beam. This solution had the added feature of spreading the stopping distribution along the beam direction, which allowed for background suppression by requiring the photon and positron to originate from the same point in the target.

To achieve a sensitivity of 10^{-13} in a reasonable time, the muon decay rate was set as high as possible consistent with minimum confusion in positron tracking and acceptably low dead times. The experiment was positioned in the LAMPF stopped-muon channel and set to accept the full muon beam. The anticipated muon decay rate constrained the positron detector MWPC cell size to achieve acceptable occupancies.

The dominant $\mu\rightarrow e\gamma$ background comes from photons near 52.8 MeV in accidental time and spatial coincidence with a random positron emanating from another muon decaying in the target. Because the mass of the positron MWPCs was very low, the most likely source of these photons was from the internal bremsstrahlung (IB) process $\mu\rightarrow e\gamma\nu\bar{\nu}$. Also high energy photons could be generated by positron annihilation along its orbit. The IB process has a very low probability of producing photons with energies close to 52.8 MeV, so good photon energy resolution provided a particularly important background rejection factor. Furthermore, because the magnetic field confined charged particles to the central region, the photon detector was expected to be very “quiet” in the presence of a high muon decay rate. This naturally led to an event trigger that required a single high energy photon.

Nonetheless, the trigger rate in the photon detector was expected to be ~ 2 kHz, which would be too high to allow all of these events to be written to tape. Therefore an additional software filter was needed to ascertain whether there was sufficient information in the photon spectrometer and

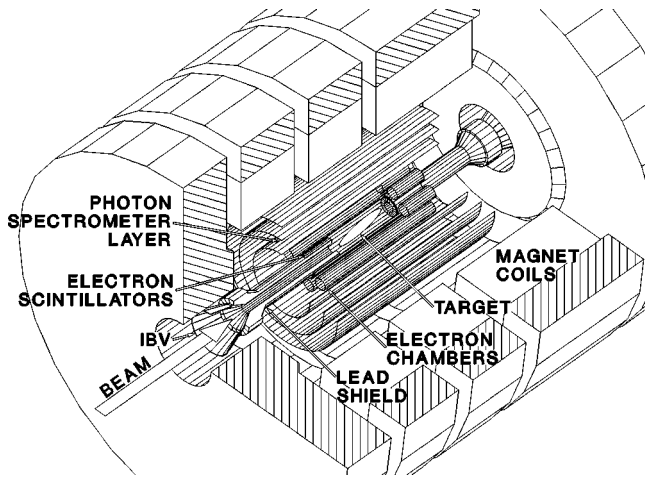


FIG. 1. A schematic view of the MEGA detector.

then the positron spectrometer to support a possible $\mu \rightarrow e\gamma$ hypothesis. This on-line filter ran in a system of computers that were programmed with fast, reliable code intended to make decisions either to keep or discard triggers. The requirement on processing speed was driven by the need to analyze all triggers from a LAMPF pulse and write the selected candidate events to tape in the ~ 8 ms period between pulses. The requirement of high reliability mandated extensive testing of the on-line code with a well-developed Monte Carlo (MC) simulation package prior to its implementation in the experiment.

The on-line filter was designed not to reject many $\mu \rightarrow e\gamma$ signal candidates, and therefore, the data written to tape would likely include large numbers of events that were not consistent with a $\mu \rightarrow e\gamma$ hypothesis. Off line, the data were to be studied with a series of increasingly more rigorous, and more time-consuming, analyses, each reducing the volume of data, and finally retaining only those events that were highly probable $\mu \rightarrow e\gamma$ candidates.

The accuracy of the experiment depended on regular and extensive temporal and spatial calibrations to assure that the test of time coincidence and the requirement for precise spatial tracking were not systematically compromised. The temporal and spatial accuracy was affected by a wide range of environmental parameters and apparatus characteristics, which needed to be monitored in coordination with the event information saved to tape. Moreover, these calibration data required substantial subsequent analyses to assure the accuracy and reliability of the $\mu \rightarrow e\gamma$ search.

III. EXPERIMENTAL DETAILS

A. Overview

Figure 1 shows a schematic view of the MEGA detector. Both the positron and the photon spectrometer systems were contained within the 1.5 T magnetic field produced by a superconducting solenoid magnet. A surface-muon beam from the LAMPF stopped-muon channel entered the detector along the axis of the superconducting solenoid. The beam stopped in the elliptical target foil located at the center of the detector.

Positrons from muon decay followed helical trajectories in the magnetic field. They were observed by an array of eight cylindrical, high-rate MWPCs that surrounded the stopping target. The MWPCs measured the crossing of positron tracks in all three dimensions, which allowed for the determination of the muon decay point and the positron momentum. Two annular arrays of plastic scintillators, located near the ends of the positron wire chambers, provided timing information. After passing through the scintillators, the positrons entered thick lead-Hevimet annuli, where they stopped while producing a minimum of high-energy gamma radiation. Cylindrical plastic scintillators that were located inside the upstream and downstream positron scintillator arrays and beyond the lead-Hevimet annuli, “ring counters,” provided timing calibrations. The positron spectrometer had an outer radius of 30 cm, large enough to contain all the positrons that were produced by muons decaying in the stopping target.

Photons from muon decay were observed in a set of three concentric, cylindrical pair spectrometers that surrounded the positron spectrometer. Each pair spectrometer utilized two lead foils to convert high-energy photons into e^+/e^- pairs. The electrons and positrons were then tracked through a set of drift chambers to determine the energy and propagation direction of the original photons. An MWPC located between the two convertor foils determined where a given photon converted, and an array of plastic scintillators determined the conversion time.

The hardware trigger for the experiment was designed to identify high-energy photons in the pair spectrometers. Events that passed the hardware first- and second-stage triggers were read into a workstation where a partial analysis of each photon shower was performed, and then the hits in the positron spectrometer were examined to determine if the minimum number necessary to support a $\mu \rightarrow e\gamma$ hypothesis were present. If so, the event was written to tape for subsequent off-line analysis.

B. Beam

The LAMPF accelerator had a macrostructure of between 6% and 9% and a repetition rate between 60 and 120 Hz. These conditions were set by the accelerator-operations staff, and the MEGA experimenters adjusted the aperture of the channel (see below) to keep the instantaneous rate a constant to about 3%. The microstructure in the beam of 5 ns was irrelevant because it was short compared to the muon lifetime.

The stopped-muon channel at LAMPF [7] provided the muons for the MEGA experiment using a surface-muon beam [8] tune. The characteristics of the beam were a flux of $2 \times 10^8/s$, 4% muons above the kinematic end point from stopped-pion decay (29.8 MeV/c) in the production target, and a ratio of positrons to muons of 10:1. To reduce the positron flux by a factor of 100, a 20.3-cm gap by 127 cm long, crossed electric and magnetic field separator, operated at a total voltage of 200 kV, was employed upstream of the last focusing quadrupole. The beam was tuned in the last lens to enter the solenoid with as little loss as possible; the solenoid also had a strong focusing effect on the beam. In order

to produce an extended longitudinal beam spot on the slanted target, the spot was purposefully defocused to have a full width at half maximum (FWHM) of 3.5 cm (normal to the beam direction) with the solenoid at nominal current. When all beam tailoring with slits was completed, the maximum stopping rate available was $4 \times 10^7 \text{ s}^{-1}$ for 1 mA of protons incident on a 6-cm graphite production target.

The central momentum of the tune was 28.3 MeV/ c with a 10% acceptance. A very small fraction of the muons stopped in the vacuum window between the beamline and the solenoid, and their decays were used for calibrating the timing of the upstream scintillators. Following the vacuum window, a degrader foil was placed inside the heavy lead shielding upstream of the target. The degrader thickness was chosen so that 75% of the muons stopped in the slanted target. The balance propagated to a foil that was inside the downstream shielding. Essentially all of the remaining muons stopped there, and their decays were used for calibrating the timing of the downstream scintillators. At this momentum, the estimated π/μ ratio at the detector (or separator) was 3×10^{-9} , and residual positrons that passed the separator were focused by the solenoid and went harmlessly through the apparatus.

The procedure for calibrating the number of muon stops involved several steps. Initially, with the magnetic field off, a beam of muons and positrons was brought into the center of the magnet. The particles passed through a thin ion chamber, a 0.16-cm-thick scintillator 10 cm downstream, and a 1.3-cm-thick scintillator another 10 cm downstream. The separation between these elements helped to keep the solid angle for detecting muon decay products low. With low intensity beam, the number of muons were counted in the first scintillator where they stopped, and the positrons were counted in the thicker scintillator. The sum of the energy deposition from both species was measured in the ion chamber. The contribution of the muons to the ion chamber response was then deduced by placing a degrader upstream of the ion chamber to remove the muons. Next, the field was turned on, with the ion chamber (electric field parallel to the magnetic field) upstream of a surface barrier Si detector, and the ratio of muons to positrons was measured with the field on but at low rate. Finally, with the field on, the ion chamber was placed substantially upstream of a target that stopped all the muons in the beam. The count rate of several of the upstream positron timing scintillators, which detected muon-decay products, was compared to the ion chamber charge. The ratios were observed to track linearly. Thus a calibration of the upstream positron scintillators to the muon-stop rate was made. A comparison of the acceptance of these scintillators to a MC simulation agreed to 5% under the assumption of 97% muon polarization at the time of their decay. The integrated counts in the positron scintillators were then monitored throughout the data acquisition to extract the total number of stopped muons. The stability of muon counts in these scintillators was about 1% over the lifetime of the experiment.

C. Magnet

The MEGA detectors were located inside a large-bore superconducting solenoid magnet. This magnet was originally

used in the Large Aperture Solenoidal Spectrometer at SLAC [9]. For MEGA, only 3 of the original 4 superconducting coils were used and the large opening in the downstream iron pole piece was filled with iron except for a small hole along the axis. The solenoid had a clear bore diameter of 1.85 m and a clear bore length of 2.89 m. The superconducting Cu-Nb coils were immersed in a 4000 liter liquid helium bath during operation; they carried 1178 A with a current density of $\sim 4000 \text{ A/cm}^2$, which produced a 1.5 T central field.

Prior to inserting the spectrometers, the magnetic field was measured on a 5.1 cm grid using Hall probes, which were calibrated in a uniform field measured with an NMR probe. The principle component of the cylindrical magnetic field was along the incoming beam direction, and varied by $< 3\%$ within 1 m of the magnet center along the central axis, with larger variations at increasing distances off axis. During data acquisition, the current in the magnet was held constant to $< 0.1\%$. The detailed field map was tabulated for use in data analysis.

D. Target

The muon stopping target [10] consisted of a planar sheet of 0.1 mm thick Mylar oriented such that the normal to the target plane was inclined at 83° with respect to the incident muon beam. This Mylar target was supported in space by rigid attachment to the inside walls of a 13 μm thick Mylar cylinder, 7.6 cm in diameter, giving the target a planar elliptical shape. The length of the target along its major axis was approximately 50 cm. The supporting cylinder was filled with helium gas and was maintained in its rigid shape by a 20 torr differential helium gas pressure. In this inflated form, the target was measured to be flat, with deviations from flatness less than $\pm 1 \text{ mm}$.

The inclined thickness of the target as seen by the incoming beam was sufficient to stop 75% of the muons, passing only those that underwent significant multiple scattering. By contrast, the thickness presented to outgoing positrons of interest was small, thereby introducing minimum energy loss, multiple scattering and annihilation. The target inclination also spread the muon stopping distribution over a broad range in z , enhancing the ability to distinguish between the separate origins of photons that were produced in random coincidence with positrons.

Because the target was passive, the first point where the trajectory of a positron was measured was typically several centimeters away from the muon-decay point. Therefore, the vector momentum of the positron at the muon decay was determined from the intersection of its observed helical track with the target plane. This made precise knowledge of the target location critical. The position of the target when mounted in the spectrometer was determined by direct visual measurements, based on a grid pinned on the target surface. Approximately 100 points on the target were measured in all three coordinates using survey instruments. Their locations formed a plane with a fitted χ^2 of 1.1 for errors of 1 mm on the space points. The absolute location of the target was mea-

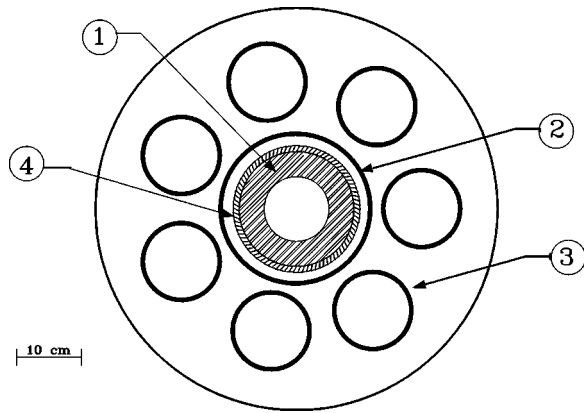


FIG. 2. An axial view of the positron spectrometer showing (1) the lead and Hevimet terminus for the positrons, (2) the Snow White MWPC, (3) the dwarf MWPCs, and (4) the positron scintillators. The outer circle represents the tension shell.

sured with the same precision when the target was in place for data acquisition.

E. Positron spectrometer

The positron spectrometer [11] consisted of a large central cylindrical MWPC (called Snow White) and seven smaller cylindrical MWPCs (called dwarfs) as shown in Fig. 2. The size, position, and internal design of these chambers were chosen on the basis of MC studies to keep the occupancy of the individual elements to $\sim 25\%$ with particle fluences of $4 \times 10^4 \text{ mm}^{-2} \text{ s}^{-1}$, so as not to confuse the pattern recognition. (An original design of 3 concentric cylindrical MWPCs failed the occupancy requirements.) The overall diameter (60 cm) of the positron spectrometer was large enough to keep all orbiting positrons from entering the photon spectrometer due to the 1.5 T solenoidal magnetic field. The length of the chambers was chosen as 126 cm to match the solid angle acceptance for the $\mu \rightarrow e \gamma$ signal within the photon spectrometer.

To minimize multiple scattering and to reduce the production of high-energy photons, the chambers were built with an effective thickness of 3×10^{-4} radiation lengths, including the thickness of the cathode foils, the gas in the chambers, and the wires. The design avoided structural supports in the MWPCs anywhere in the detector volume where positrons might pass. Accordingly, the wire tension was maintained by a cylindrical support, the “tension shell,” external to the positron orbit, and the cylindrical shapes of the thin cathode foils were maintained by differential gas pressure. The chamber anode wires were too long to be electro-mechanically stable under high voltage, so low-mass garland supports were required to mechanically divide the wires into shorter regions.

The basic layout of a dwarf chamber is shown in Fig. 3, and the chamber parameters are listed in Table I. The orientation of the anode wires parallel to the magnetic field minimized the number of anode cells activated by a helical positron path since the same cells would be struck multiple times in the orbit. The spacing between anodes and the separation between the anode high voltage plane and the cathode

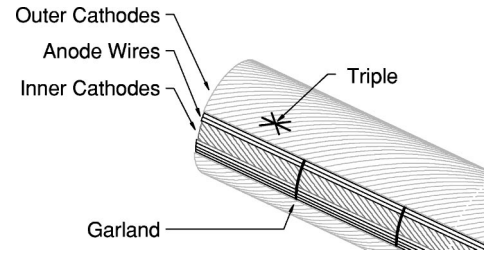


FIG. 3. A partial cut-away view of a dwarf chamber showing the anode wires between the two cathodes with counter-directed helical stripes.

ground plane were chosen to achieve the design resolutions at the decay point (2 mm in space and 0.5% in momentum) and to have acceptable occupancy rates.

A longitudinal position resolution of 4 mm for a track crossing was required to obtain better than 0.5% momentum resolution. To achieve this goal, the copper coating on the cathode foils was segmented into electrically separated, helical shaped stripes, each of which had an individual readout. To reduce occupancy rates, the stripes were separated into upstream and downstream channels by a division at the median plane. The copper coating on the Snow White cathodes was divided into stripes only over the scintillator region, leaving the copper coating in the central region unbroken except for the division at the median plane. This prevented the high occupancy rate in the central region of Snow White from obscuring the resolution required adjacent to the scintillators.

A sophisticated gas system was built to mix the chamber gases and to maintain the 20 torr differential gas pressure that was required to support the chamber cathode shapes. In addition, the gas system was used to inflate the muon stopping target support cylinder. The high occupancy rate in the spectrometer dictated that a fast chamber gas be used. A freon/isobutane mixture of 80% CF_4 and 20% isobutane achieved this goal with an ion collection time of $\sim 15 \text{ ns}$ [12]. Water vapor (0.2%) was added to the gas mixture to suppress continuous discharges. Also the inner and outer volumes that surrounded the MWPCs were filled with helium to

TABLE I. Parameters of the MEGA positron spectrometer MWPCs.

Chamber length	126 cm
Chamber radius	11.138 cm (Snow White) 5.982 cm (Dwarfs)
Wire spacing	1.3 mm
Wire type	15 μm Au-W
Wire tension	25 g
Half gap	1.778 mm
Cathode foil	Cu (200 nm) on Kapton (25 μm)
Cathode stripe width	2.7 mm (Snow White) 2.8 mm (Dwarfs)
Cathode stereo angle	29.05° (Snow White) 16.61° (Dwarfs)
Chamber gas	CF_4 (80%) + C_4H_{10} (20%)

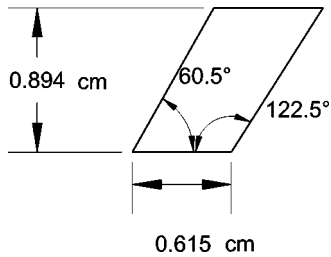


FIG. 4. Cross-sectional view of a positron scintillator.

reduce positron interactions as they passed through the spectrometer.

A LeCroy 1445 high voltage supply [13] provided the high voltage for the MWPCs. It was linked via a serial connection to a computer running the LabView [14] instrument control program. The LeCroy 1445 was chosen because it provided an exceptionally fast trip response, which was critical for these chambers, while allowing computer-linked control and monitoring. The LabView controlling program was written to allow simultaneous independent control of each of the 13 different high voltage supplies used.

The positron chamber read-out system [11] was constrained by several requirements. First, the high instantaneous rate per wire (10–20 MHz) required a wide bandwidth (~ 100 MHz) in order to resolve the chamber hits cleanly. Second, the high flux through the chambers made it necessary to run the MWPCs at relatively low gas gain ($\sim 5 \times 10^4$), thus requiring highly sensitive electronics with extremely low noise levels. Finally, the limited real estate available for the chamber-mounted preamplifiers and the large number of channels restricted the design to a bare minimum of components. Preamplifier outputs were sent to rack-mounted amplifier-discriminator cards within the experimental cave. Discriminator outputs were routed to Phillips 10C2 [15] FASTBUS latches for read out.

Positron timing information was obtained from the 174 plastic scintillator strips that formed two cylindrical barrels. Each scintillator was a 30-cm-long rod with a trapezoidal cross section (see Fig. 4). This shape was chosen to minimize the number of scintillators crossed by a single spiraling positron. Each scintillator was individually wrapped in aluminized Mylar foil for optical isolation. The end opposite the light guide connection was blackened to prevent multiple reflections. The scintillators were closely packed into a barrel on the outside of the lead-Hevimet absorber. One scintillator was missing to allow space for a tube to supply gas to the space between the target and Snow White. Each scintillator was connected to a phototube with a 1.8-m-long optical fiber light guide so the phototubes could be located in a shielded enclosure outside the magnet. Signals from the phototubes went to FASTBUS analog to digital converters (ADCs) and to discriminators, which fed FASTBUS time to digital converters (TDCs) [15] and a logic OR for trigger purposes.

An unexpected property of the detector, combined with the response of the electronics, limited the rate capability of the experiment. As noted above, anode cells oriented parallel to the magnetic field could be crossed multiple times by a helical positron track. The cathodes also could experience

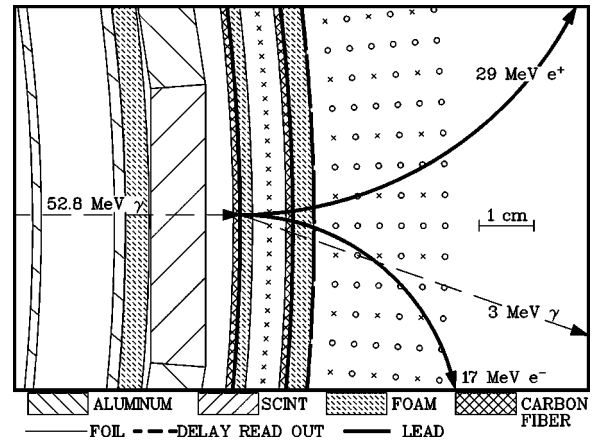


FIG. 5. A cross section of a pair spectrometer layer, showing the aluminum support cylinder for an inner layer, and the timing scintillators, conversion cylinders, MWPC and drift detectors for the next outer layer. A typical conversion in the first conversion cylinder is shown.

multiple crossing of the track when the positron helical orbit intersects the same helical cathode cell on a later crossing. If the same read-out channel was hit repeatedly within the resolving time of the electronics (20 ns), as happened routinely for the anodes when positrons spiraled nearly perpendicular to the magnetic field, the pulses piled up. This pile-up greatly increased the dynamic range requirement on the electronics. The channel-to-channel cross-talk isolation of the preamplifier cards was measured to be 30 dB. However, if a great deal of energy was deposited near the same wire by several crossings of a positron, a very large pulse occurred that induced cross talk on neighboring wires. Such an event had a small probability, but at high muon stopping rate, this small probability was multiplied by the large number of channels in the entire system so that there was cross talk in nearly every trigger. To reduce the effect of the cross talk, both the muon stopping rate and the gain of the chambers were reduced below design values. The result was a limit on the instantaneous muon stop rate of 2.5×10^8 Hz, and average anode and cathode efficiencies of 95% and 85%, respectively.

F. Photon spectrometer

The photon detector [16–19] consisted of three independent, concentric, cylindrical pair spectrometers, which surrounded the positron spectrometer. Pair spectrometers were chosen for detection of the decay photons because they provided some directional information, and comparatively, the best possible combination of energy, timing, and spatial resolutions for the 52.8 MeV photons of interest. Increased conversion efficiency, while maintaining good energy resolution, was achieved by using a system of multiple spectrometers. The detector had fine granularity, which allowed high data rates with low event pile-up.

A cross sectional view of a pair spectrometer sector is shown in Fig. 5, and Table II gives radial dimensions of the components. Each pair spectrometer was about 175 cm in axial length. It contained two cylindrical, lead convertor foils

TABLE II. Components of the photon pair spectrometers. All radii are in cm.

COMPONENT	Layer 1	Layer 2	Layer 3
Scintillator			
Number of scintillators	40	60	80
Radius	32.0	47.9	63.4
Lead conversion cylinder			
Radius of 1st	33.6	49.5	64.9
Radius of 2nd	34.5	50.4	65.8
MWPC			
Number of wires	416	640	832
Radius	34.2	50.1	65.5
Drift chambers			
Number of wires	208	320	416
DC1 radius	35.3	51.3	66.7
DC2 radius	36.1	52.1	67.5
DC3 radius	36.9	52.9	68.3
DC4 radius			71.1
Aluminum support cylinder			
Radius	47.6	62.8	88.3

between which was a MWPC. Just outside the converter cylinders was a set of cylindrical drift chambers to track the conversion pairs. A scintillation barrel, placed inside the conversion layers, timed the traversal of the then back-traveling lepton pairs, and also measured their trajectory diameters, which were proportional to their transverse momenta. This information was used in the trigger to select only the conversion of high-energy photons. The scintillators were also used to determine the time of conversion and to establish the time reference for the drift chamber TDCs.

The tension of the chamber wires in each layer was balanced by the compressional resistance of a rolled and welded aluminum cylinder, 2 mm in thickness, which was placed beyond the maximum turning radius of reconstructable e^+e^- tracks. This cylinder also acted as the outer gas barrier for the drift chambers.

Each of the three spectrometer layers contained 3 conventional, cylindrical drift chambers with individual drift cells approximately 1 cm long and 0.8 cm high. A fourth set of drift chambers was added to the outer layer. These cells, except for the inner drift chamber of each layer, were defined by sense wires at the center of the cell, and field wires positioned at the corners and between each sense wire. In the case of the inner drift chamber, the outer surface of the conversion cylinder formed an equipotential on which a delay line [19] was positioned under each sense wire.

A typical event had a pair conversion in either the inner or outer lead conversion foil, each being 0.045 radiation lengths. If the conversion occurred on the inner foil, the pair traversed the MWPC and the outer foil layer before entering the drift chamber region. Thus, a signal in the MWPC at the vertex of an e^+e^- pair identified these specific events. The e^+e^- pair curled in opposite directions through the drift

chamber region; their trajectories were used to determine the transverse component of their momenta. After making circular arcs through the drift chamber region, the pairs then passed back through the conversion cylinders, the MWPC, and the scintillator. Depending on energy loss and multiple scattering in the scintillators and the aluminum support cylinder, the pairs could continue to spiral in the magnetic field, although with smaller radii, so that in cross section the trajectories did not overlap. Tracking information was utilized only from the first pass of the leptons through the drift chambers, although multiple scintillator hits were used to improve event timing.

The z location of the pair vertex and the position where each lepton spiraled back through the conversion cylinder were measured with the delay lines. These points determined the polar (dip) angle of the photon with respect to the cylinder axis. The dip angle was combined with the measurement of radius of curvature of the leptons in the magnetic field to compute the full energy of the photon and its propagation direction. The position of a drift-cell crossing was determined with a precision of about 200 μm in the direction transverse to the magnetic field and about 1 cm in the z direction. The time of the photon conversion was obtained by correcting the time appearance of the scintillator signals for the flight time of the leptons.

The delay lines were composed of an etched laminate of 34 μm thick copper sandwiching a 75 μm thick polyamide foil. The signals were read differentially at each end by a voltage preamplifier feeding a constant fraction discriminator, and the resulting signals were then gated into a FASTBUS TDC to record the timing information from each delay line. Each line was thus equivalent to a distributed parameter transmission line, and because the resistance was not negligible compared to the characteristic impedance of the line, the signal rise time degraded and the pulse amplitude decreased as a function of distance along the line. Although constant fraction discriminators were used to reduce the effect of the time walk of the signal, this effect was, nonetheless, a significant problem, and limited the spatial resolution to about $\delta L/L = 0.5\%$ for the approximately 175 cm long lines.

G. Internal bremsstrahlung veto

The dominant source of photon background was the IB process. High energy photons emitted in IB have a high probability to be accompanied by a low energy positron. In contrast the probability of low energy positrons from normal muon decay is small. The IB positrons were easily and cleanly detected in coincidence with high energy photons in the Crystal Box detector [5]. The MEGA detector was instrumented with internal bremsstrahlung veto scintillators (IBVs) mounted on the surface of the pole tip penetrations, whose purpose was to veto low-energy positrons emitted in the IB process. In the 1.5-T magnetic field, 0- to 5-MeV positrons were constrained to follow the field lines and thus hit the 30-cm-radius penetrations in the magnet iron surrounding the beam. The time of arrival of these positrons ranged from 20 to 80 ns after the muon decay, as determined

TABLE III. A comparison of MEGA trigger rates at full beam intensity (in Hz).

Item	Per μ stop	Instantaneous	Average
μ stop	1.	2.6×10^8	1.3×10^7
First-stage trigger	1.2×10^{-4}	3.1×10^4	1.6×10^3
Second-stage trigger	6.4×10^{-5}	1.7×10^4	8.3×10^2
Photons > 47 MeV ^a	8.5×10^{-6}	2.2×10^3	1.1×10^2

^aReconstructed in off-line analysis from data with the on-line filter for the positron spectrometer temporarily disabled.

by the initial dip angle. During the development of the beam for the experiment, it was discovered that beam halo prevented IBV counters from being effective upstream. Consequently four counters were mounted in the top, bottom, left, and right positions, which were only used to monitor the beam position. As no muon beam reached the downstream IBV location, it was lined with 18 counters, arranged azimuthally, to intersect all positrons in this energy range originating in the target with a positive value of p_z .

H. Trigger and data acquisition

The first-stage trigger [18] used the fact that the sum of the diameters of the circular trajectories of the conversion pair measured the transverse component of the photon momentum. MC studies of photon yields were used to select hit patterns in the MWPCs and scintillators of the photon spectrometers for coding into the first-stage trigger electronics. Each photon pair spectrometer operated independently, producing its own first-stage trigger. The trigger required that at least two scintillators were hit in spatial coincidence with three groups of MWPC cells, corresponding to a minimum width consistent with a ~ 37 MeV/ c transverse photon momentum (p_T). Thus, the trigger cutoff was determined by p_T and not total photon energy. However, p_T was strongly correlated with total photon energy because of the geometry of the detector.

The purpose of the second-stage trigger was to reject events that satisfied the first-stage trigger, but did not produce tracks in the drift chambers, or did not have the sufficient number and pattern of hits in the drift chambers to reconstruct a photon event. It imposed additional constraints on a candidate photon event based on hit requirements in the drift chambers, to reduce substantially first-stage triggers caused by accidental coincidences between two lower-energy photons, or true high-energy photons produced by conversions in either the photon scintillators or the aluminum cylinders. Each photon spectrometer layer had its own second-stage trigger module. Table III compares various trigger rates at full beam intensity.

An electronic controller, the “routing box,” was used to coordinate the triggers from all three layers with the dead time of the data acquisition system, and was the central control module for the trigger system. It combined the first-stage trigger results with selected additional signals to form a desired set of triggers, then routed the gate outputs to the group of FASTBUS modules that were required to read out the

event. It also kept track of the FASTBUS-module busy signals, sent start signals to the second-stage trigger, monitored the result of the second-stage trigger decision, and sent out a fast clear or transfer-to-memory signal (i.e., keep the event for subsequent read out) to the appropriate FASTBUS modules following the second-stage trigger decision. All of these tasks were accomplished under computer control.

Each pair spectrometer had dedicated FASTBUS TDCs, ADCs, and latches [15] that could be read out independently to minimize the dead time. However, the positron spectrometer needed to be read out for every event, regardless of which photon layer generated the trigger. To facilitate this, the TDCs and ADCs for each positron scintillator were read by alternating between a pair of modules, designated “even” and “odd.” This allowed the data acquisition system to accept, for example, a trigger in layer 1 while a previous trigger from layer 2 was still being digitized. In contrast, the transfer-to-memory cycle of the FASTBUS latches was sufficiently fast that only a single set of read-out modules was needed for the positron spectrometer MWPCs. The typical data acquisition system dead time was $\sim 6\%$.

Since the event rate in the photon pair spectrometers was low, the number of FASTBUS interface modules was reduced by multiplexing the photon chamber signals. A scheme gating a block of these signals in the azimuthal location of the first-stage trigger minimized accidental overlap for the wire chamber signals [18].

The first-stage trigger rate as filtered by the second-stage trigger was still too high to commit all event data to permanent storage. Therefore events were entered into an eight-computer DECStation 5200 workstation farm that further filtered their number via preliminary physics analysis. Each event that contained a candidate photon with an energy $E_\gamma > 42$ MeV passed the on-line photon spectrometer requirement. Typically 27% of the triggered events passed the photon on-line pattern recognition requirements, and these events were then analyzed by the positron spectrometer on-line code ARC described in Sec. VII A. If the event also satisfied the ARC criteria, it was written to tape for subsequent off-line filtering. Typically, 15% of the events that passed the photon on-line requirements also passed ARC. In addition, a small sample (0.5%) of events that failed the on-line event filter was written to tape in order to provide a continuous monitor of the performance of the on-line filter codes.

I. Data taking procedures

Data for this experiment were accumulated during calendar years 1993-1995. Approximately every 8 h, the scintillator timing and electronic pedestal calibrations were checked. Otherwise, data were collected at the full operating rate except for the brief interruptions required for the supplementary measurements described in Secs. V and VIII.

During routine data collection, the performance of the detector was monitored in a number of ways to ensure the quality of the data. Approximately 80 separate measurements, such as room temperature, wire chamber voltages and currents, solenoid field setting, cryogenic instrumentation readouts, etc., were recorded roughly once per minute by a

dedicated computer interfaced by GPIB bus to sensors. Quantities outside preset limits caused an alarm to sound. Another system monitored quantities that were scaled and translated into quantities such as dead time, pass-through rates in the software filters, detector rates, etc. In the case of changes in accelerator parameters, the experimenters adjusted the average stopping rate by changing the channel slits to keep the instantaneous rate at 250 MHz. In addition, a graphical single event display (SED) was available for viewing the patterns of hits in the detector elements on an event-by-event basis.

Deciding that an instantaneous stop rate of 250 MHz was optimal proved to be quite challenging. This decision was made after visually studying thousands of events from the SED. As the final positron spectrometer reconstruction program was not available at the time the data were taken, the complexity of events that could be properly analyzed had to be judged *a priori*.

IV. MONTE CARLO

The MC simulation of the MEGA apparatus was based on the EGS4 [20] package, with several modifications to meet the requirements of this experiment. The geometries of the positron and photon spectrometers were coded into the simulation according to their actual construction. The detector was subdivided into single-medium regions that were bounded by up to seven surfaces (planes, cylinders, or cones). Checking geometric limits is recognized to be one of the most time-consuming tasks in any particle physics simulation, and much effort was expended to optimize this task. For example, separate sections of the code were exercised to find the intersection(s) of either a straight line segment or an arc of a helix for each type of surface. As a result the performance of the simulation was about 4 times faster than would have been achieved with a GEANT-based [21] simulation. Other special features of the simulation are presented below.

A. Event generation

Events were generated within the simulation program using one of the following processes: (1) unpolarized $\mu^+ \rightarrow e^+ \gamma$, (2) polarized $\mu^+ \rightarrow e^+ \nu \bar{\nu}$, (3) unpolarized $\mu^+ \rightarrow e^+ \gamma \nu \bar{\nu}$, (4) $\pi^0 \rightarrow \gamma \gamma$ (where the π^0 originated from $\pi^- p \rightarrow \pi^0 n$), (5) $\pi^- p \rightarrow \gamma n$, (6) e^+ with uniformly distributed momentum and direction, (7) μ^\pm with a cosmic ray energy and direction spectrum.

For the first three processes, the muon was assumed to be at rest in the thin, planar, Mylar target. For the fourth and fifth processes, the $\pi^- p$ reaction was assumed to occur with the π^- at rest within a thick cylindrical polyethylene target. Finally, the simulated cosmic ray spectrum had a $1/E^2$ energy dependence and a $\cos^2 \zeta$, zenith angle dependence.

For the muon decay modes, an option was provided to simulate the high-rate backgrounds. In the positron spectrometer, this could be done by superimposing hits from either MC simulated muon-decay positrons or real events onto the high-rate data. In the photon spectrometer, the overlay was done by including additional random hits according to

the relative frequencies that various patterns were observed during background studies. These options permitted a reliable determination of the detection efficiency as a function of beam rate.

B. Extensions to EGS4 physics

A routine extracted from GEANT was added to the EGS4 package to permit the tracking of muons, including beam muons and energetic cosmic rays, within the apparatus. (Cosmic rays were used in detector alignment and position resolution studies, for example.) Muons were treated as long-lived ionizing particles; neither decays nor nuclear interactions were considered.

In addition to the limitations on the step size of charged particles imposed by EGS4 and the geometry of the MEGA apparatus, the ionization energy loss per step was not allowed to exceed 5% in the positron spectrometer or 2% in the photon spectrometer.

For the traversal of charged particles through thin media — gases or very thin solids — the mean number of elastic scatterings N often falls below the value of 20. Thus the Molière parametrization of the scattering angle is no longer valid. To account properly for single and plural scattering in such cases, the Molière parametrization was replaced with a new algorithm, if the mean number of scatterings was below 25. In this new algorithm, the number of scatterings in one step was sampled from a Poisson distribution with mean N . Then this number of single scatterings were sampled from a screened Rutherford scattering distribution and convolved to give the overall scattering angle. The resulting distribution merged smoothly into the Molière approximation for $N \geq 25$.

The *average* restricted energy loss by charged particles in EGS4 was replaced with a new algorithm that incorporated fluctuations. This was required to model accurately the energy resolution of the spiraling positrons in the positron spectrometer and the fluctuations in pulse height detected by the MWPCs. If the Molière number of scatterings in one step was smaller than 25 or if the charged particle was passing through the chamber gas of an MWPC, the restricted energy loss was calculated using the method of Talman [22] to sample the energy loss due to resonant as well as non-resonant ionization of electrons from the various atomic shells of the element(s) of the media. (Resonant ionization results in an electron-ion pair where the liberated atomic electron has no kinetic energy; non-resonant ionization results in an electron-ion pair where the liberated electron has kinetic energy below the EGS4 discrete-tracking cutoff of 25 keV.) As a side benefit, the individual sampled ionizations within an MWPC cell were used to generate the detected pulse — including fluctuations in pulse height and arrival time at the anode. If the Molière number of scatterings exceeded 25 — i.e., when traversing thick media — the restricted energy loss was sampled from a set of eight tabulations of the Vavilov distribution. These tabulations were used to simulate energy loss in the photon spectrometers, independent of the thickness of the media.

C. Signal generation

Signals from energy deposited in the detector elements were recorded in simulated ADCs, TDCs and latches exactly matched to the data format of the actual apparatus. Additional simulation-specific information keyed to these signals was written to help identify in detail the history of each event and debug the reconstruction and analysis programs.

The signal from energy deposited in each positron scintillator was propagated, with a time delay, to the phototube and then recorded in an ADC and TDC. TDC dead times were simulated by imposing a time window from a previous over-threshold hit so that the second of two close-together hits was lost. Each TDC had a programmable pulse-height threshold that was tuned to match the detection efficiency of the actual scintillator. Each ADC had a threshold (for zero suppression) to match the behavior of the real ADCs.

Electrons released by energy deposition in each positron spectrometer MWPC cell were propagated to the anode wire. The cell boundaries were tilted from radial by about 17° due to the Lorentz $E \times B$ effect on the drifting charge in the chamber gas. The arrival time of the avalanche — usually but not always from the point of closest approach of the trajectory to the anode — determined the initial time of the anode and cathode signals. The pulse on the nearby inner and outer cathodes was the spatial image of the anode pulse with a Gaussian shape and an rms size determined by the chamber half-gap and the cathode stereo angle. These initial pulses on the anode and cathodes were then propagated with delay to the readout end of each element and turned into an electronic pulse shape with a base width of about 25 ns. For each event, the electronic pulses on all channels were superimposed to account for possible pulse pile-up due to recurring hits on the same channel from multiple loops, as well as uncorrelated hits at high beam rates. The resulting signal was discriminated using a threshold that was matched channel by channel, then checked to see that it was within the time gate that had been started by the event trigger. Signals that were above threshold and in time were recorded in simulated latches.

In the photon spectrometer, the signal from energy deposition in a scintillator was propagated to each end and recorded in simulated TDCs and ADCs. Drift chamber, delay line and MWPC hits were simulated by determining the earliest arrival of an electron cluster at the preamplifier mounted on the end of a sense wire or delay line. At the end of the event, the outputs of the ADC for each scintillation channel and the TDC for each scintillation or wire chamber channel that was above threshold were smeared to account for both pulse-height independent and pulse-height dependent resolution effects. Background noise hits in the scintillators, MWPCs, delay lines, and drift chambers were superimposed on the event. The event was then examined to determine if the hits were sufficient to pass the hardware first- and second-stage trigger requirements. If so, the event was saved after adjusting all TDC times so that the hardware first-stage trigger defined the effective zero time. (During the simulation, $t=0$ was given by the muon decay time.)

TABLE IV. Wire chamber and scintillator efficiencies by layer and by year.

Wire chamber	Efficiencies				
	Layer 1		Layer 2		Layer 3
Year	1995	1993	1995	1993	1995
MWPC	98.9	99.1	100.	99.1	97.5
DC1	97.1	96.8	97.0	97.6	96.4
DC2	97.5	98.8	99.5	95.9	95.6
DC3	97.2	98.5	96.2	95.9	96.1
Scintillators	95.1	96.5	96.8	97.5	87.6

V. DETECTOR CALIBRATIONS

A. Photon detector drift times

The magnetic field significantly influenced the drift time in the wire chambers. Given the approximate electric and magnetic fields and the equilibrium drift velocity, the Lorentz angle for the drifting electrons was approximately 37° . This large drift angle increased the drift time by about a factor of 2, and reduced the ionization charge collected on the wires. In addition, some of this charge leaked between adjacent drift cells for certain track geometries. Nevertheless, MC simulations demonstrated that the equal-time drift contours were approximately circular, although charge deposited in drift-cell corners remained trapped for long periods [16]. These simulations also indicated a slight angular asymmetry of the contours. This effect was ignored in the analysis of the drift-distance vs drift-time data for all three wire chambers of all three layers. The drift time distributions were fit by one quadratic function:

$$d = v_0 T + a_0 T^2. \quad (1)$$

The parameters of the fit, $v_0 = 0.0049$ cm/ns and $a_0 = -9 \times 10^{-6}$ cm/ns², were very close to those obtained from the MC simulation, averaged over all wire chambers and layers. By this procedure the distance from the drift wire to the tangent of the track position was located within 0.2 mm rms, which was more than sufficient for the experiment, as resolutions were dominated entirely by the axial, rather than the azimuthal, position measurement.

B. Photon wire chamber and scintillator efficiencies

Representative wire chamber efficiencies (magnetic field on) are given in Table IV, as measured by cosmic rays tracked through the system. The uncertainties in these numbers are about 1%. The table shows that the wire chamber efficiencies were relatively stable from the beginning, 1993, until the end, 1995, of the experiment. Scintillator efficiencies were somewhat lower than expected, and layer 3 in particular developed several dead channels, resulting in its lower efficiency. Layer 3 was added to the experiment after the cosmic ray data were taken in 1993, so there were no 1993 data for comparison.

C. Spectrometer alignment

It was necessary to determine the location of the positron spectrometer elements relative to the established MEGA coordinate system in order to reconstruct the positron tracks precisely. The spectrometer coordinate system was defined to have its z axis aligned with the cylindrical axis of Snow White. The positive direction pointed downstream along the muon beam. The x axis was defined to lie along the centers of Snow White and the MWPC, dwarf No. 1, which was approximately horizontal. The y axis was directed upward completing a right-handed coordinate system. The axis of Snow White was assumed to lie along the axis of the solenoidal magnetic field, and no evidence of misalignment was found. The (0,0,0) location was defined to be on the Snow White axis at the center of the symmetric upstream-downstream helical cathodes.

The spatial alignment of the spectrometer components was accomplished using cosmic ray tracks, with and without the magnetic field, and positron helical tracks from muon decays in the target [11]. The various relative orientation parameters were adjusted to optimize the χ^2 fit to a large ensemble of such tracks. The process was sequential, and began with an alignment of the axial anode wires in the seven dwarf MWPCs relative to the anode wires in Snow White. This alignment required only fits to the cosmic ray tracks as viewed along the z axis, and resulted in the x - y position of the centers of each of the dwarf chambers. It also determined the azimuthal rotation angle of the anode wires around the cylinder axis for each dwarf chamber. Once the full set of 21 parameters was determined, the axial (z) alignment was begun. A track crossing the MWPC produced an anode cluster and an inner and an outer cathode cluster. By rotating the inner and/or outer cathode cylinder, the intersection in z along the two cathodes was brought into agreement. This determined the relative alignment of the cathodes in the eight MWPCs. The inter-cathode alignment between the dwarf chambers and Snow White was established by “sliding” each dwarf cathode inner and outer pair along the z axis to optimize the track fits.

In all, 36 alignment parameters were determined for the positron spectrometer. It was initially assumed that the anode wire spacing around the cylinder axes was sufficiently regular that wire-by-wire adjustments would not be required. During the alignment process, however, it was discovered that, while the spacing between neighboring wires was always well within the $75\ \mu\text{m}$ chamber winding tolerance, there were regions where many sequential wire spacings were systematically large or small. The cumulative irregularities led to misalignments of some MWPC wires by a significant fraction of a cell. Therefore, wire-by-wire azimuthal position tables were constructed for the anode wires [11] and employed to position the wires properly in the positron spectrometer MWPCs.

The alignment of the photon spectrometer relative to the positron spectrometer was determined using helical cosmic ray tracks. Photon scintillators were used as a trigger and coincident wire chamber information in the photon and positron spectrometers was read. For the azimuthal alignment, circle segments, seen when viewed along the z axis, were

reconstructed using wire chamber hits from the positron and the photon spectrometers. The track fits were optimized by varying azimuthal rotation offsets and the (x,y) location of the cylinder axes for the wire chambers in each of the three layers of the photon spectrometer. The rotational corrections for the three photon spectrometer layers were found to be $<15\ \text{mr}$ and in good agreement with optical survey results. In addition, a test was made for misalignment of the cylinder axis of the photon spectrometer layers with respect to the z axis of the coordinate system; the corrections were found to be negligible. All of the alignment parameters were included in the detector database and employed in the track reconstruction programs.

D. Delay line calibrations

Delay lines were used to determine the axial position of events in the pair spectrometers. Since the relation between position along the lines and propagation time was observed to be very linear, the axial position was determined by the propagation velocity of the signal, “slope,” and the time-zero offset, “intercept,” for each line. These constants were extracted by analysis of cosmic tracks through the complete MEGA detector. With the field on, cosmic rays passed through the pair spectrometers and positron chambers, and 3-dimensional event positions extracted from the positron chambers were used to project the trajectory arcs through the pair spectrometers. As the position in each pair spectrometer was determined from the innermost layer outward, the calibration constants for each delay line and drift chamber were obtained.

It was possible for ionization along a chamber track to cross cell boundaries and produce signals on adjacent delay lines, but events were also observed that appeared to be induced on adjacent lines by electronic cross talk. These events were removed for the calibration analysis. The propagation velocity along the line was $0.654\ \text{cm/ns}$ for single-line signals and $0.634\ \text{cm/ns}$ for double-line signals [19].

E. Positron spectrometer MWPC efficiencies

A measurement of the positron spectrometer MWPC performance was obtained using cosmic ray trajectories [11]. The trajectories were reconstructed from the photon spectrometer wire chamber hits and then projected through the positron MWPCs. These tracks were used to measure the individual efficiency of every anode and cathode in each of the eight MWPCs. Plots of these efficiencies were used to reveal inoperative electronics channels, misaligned connectors, and overall MWPC performance. For data analysis these efficiencies were superseded by high statistics efficiency studies carried out with positron tracks from low rate stopped muon decays in the target, as described in Sec. VIII A.

From the individual anode and cathode efficiencies, the average anode and cathode efficiency in each MWPC was computed at various anode high voltage settings. Plots of these average efficiencies were used to establish the optimum operating voltages and demonstrate that the MWPCs were on plateau. A further detailed examination of the individual

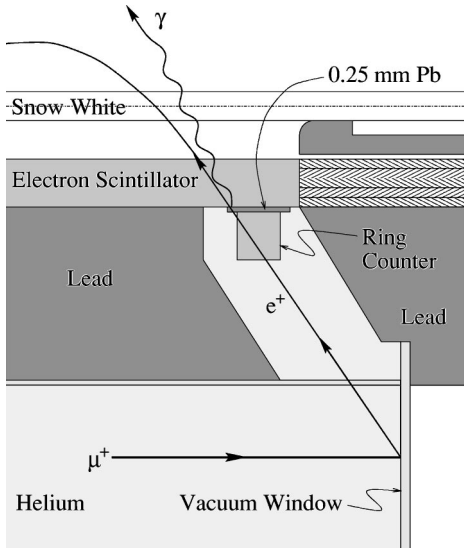


FIG. 6. The location of the downstream ring counter.

channel efficiencies as a function of high voltage gave evidence for non-uniformities in the shape of two of the MWPCs. These difficulties were addressed by using multiple high voltages applied to different regions of these two MWPCs.

The average anode and cathode efficiencies for each MWPC were measured as a function of the delay between the photon spectrometer trigger and the gate applied to the positron MWPCs, thus establishing the correct gate timing in the trigger. In addition, average anode and cathode efficiencies were employed to set the optimum value for the thresholds on the amplifier-discriminator cards for the MWPCs.

F. On-line timing

The positron-photon time difference, $t_{e\gamma}$, was calculated in terms of time intervals that were measured by the apparatus, so that a value of zero corresponded to coincident emission from the target. Part of this calculation involved the subtraction of the invariant time intervals due to fixed electronic delays or signal propagation in detector elements and cables. These equal-time offsets were measured in special timing calibration runs that determined the offset for each scintillation channel, and monitored its drift as the local environment changed. Separate equal-time offsets were recorded for the even and the odd read-out TDCs on each positron scintillator.

The on-line time calibration used a pair of dedicated ring-shaped scintillators located at the far ends of the upstream and downstream beam pipes and inside the positron scintillator barrels (see Fig. 6). Each counter was instrumented to record the hit times at both azimuthal ends of the ring (“high ϕ ” and “low ϕ ”). A small slot in the lead beam pipe permitted some positrons produced in muon decays on the vacuum window to hit the ring counter. Some of these positrons then radiated a photon; the bremsstrahlung probability was enhanced by wrapping the outside of each ring counter with lead tape. The positron nearly always hit a positron scintillator, while the radiated photon entered the MEGA de-

tektor roughly along the slot, then converted into an e^+e^- pair or Compton scattered in the photon spectrometer.

The scintillator timing calibration events were triggered by the coincidence of a ring counter and any photon scintillator. In this restricted geometry, the typical flight paths of the photon and positron were fixed on average so that the centroids of the time distributions were constants for the struck scintillators. Offsets were determined channel by channel relative to the ring counters. Global offsets between the upstream and downstream ring counters and between the even and odd positron scintillator TDCs were determined from averages over the photon scintillators.

Timing calibration runs were taken once every 8 h during the course of the data runs, and new timing constants derived from these runs were loaded into the on-line event filter programs once per day. This ensured that the timing constants in use by the on-line filter at any given time were accurate to $\lesssim 1$ ns.

VI. PHOTON EVENT ANALYSIS

A. Event reconstruction

The photon spectrometer reconstruction algorithms needed to find e^+e^- pairs resulting from the conversion of a photon, and to determine the photon energy, propagation direction, conversion point, and conversion time from the tracks produced by the pair. When viewed along the magnetic field direction, the e^+ and e^- traveled in circular orbits, activating drift cells along their paths. As the pair passed through detector material and lost energy, the radii of the orbits decreased. These characteristics defined the patterns of cells that were hit in a typical photon conversion. The transverse momenta of the electron and positron were determined by fitting the hit drift cells to circular paths, and the longitudinal momenta of the particles were calculated from the z values at the vertex and edges of the event as measured by the delay lines. The time of the photon conversion was determined from the times of scintillators that were hit in each circular orbit of the particles.

Pattern recognition was an important consideration during the design of the photon spectrometer hardware, so parameters such as MWPC wire spacing and drift cell sizes were determined from consideration of mechanical and physical tolerances, ability to reconstruct events and system cost. Consequently, many photon events were straightforward to analyze. The tracks from the e^+e^- pair formed clean circles of decreasing radii in a view of the detector perpendicular to the drift wires. The occupancy rate in the drift chambers, coupled with the active gating scheme mentioned in Sec. III H, produced relatively clean events. The challenge was to develop reconstruction algorithms to automate what the eye could see, in spite of the wide statistical variations from event to event.

The reconstruction process passed through several stages of computer code. Initially candidate events were found by looking for patterns of hit cell coordinates that were similar to typical event patterns found in MC simulations. The cells corresponding to the best guess for those hit during the initial arcs of the conversion pair were then tagged. Since each

member of the pair passed through a substantial amount of material, subsequent arcs were only useful for helping to improve the timing resolution for the photon conversion. Equal time contours were found for each hit cell as described in Sec. V A. The drift time information for these cells was then used in a non-linear least-squares fitting routine to determine the best circle fit for each member of the pair. Constraints on the circles were included to ensure that the pair originated at a common location. By incorporating the z information for the tracks, the location, $(R_\gamma, \phi_\gamma, z_\gamma)$, and time, T_γ , of the photon conversion and the vector momentum of the photon were determined. Appendix A gives a description of the analysis routines.

B. Background

Background events arose from a number of sources including reconstruction errors, two low energy photons that converted close together in space and time and Compton scattering of a photon. The pattern recognition algorithms eliminated most ($\approx 90\%$) of the Compton events. Most of the events where two lower energy photons converted and were reconstructed as a single high energy candidate were eliminated by additional checks on the number of cells that were hit outside of the reconstructed photon shower. However, some candidate events survived due to these background sources, which produced a high energy tail on the reconstructed photon energy spectrum. The final step in the reconstruction process was a visual examination (“hand scanning”) of candidate events. The sample chosen for hand scanning included all events that passed the initial $\mu \rightarrow e\gamma$ cuts imposed in the off-line filter. Interspersed with this sample were MC events, which were used to determine the efficiency of the hand scanning process. Most background events that survived the filter cuts were removed from the final event sample during the hand scanning process.

C. Performance

The overall efficiency of the photon spectrometer to detect 52.8 MeV gamma rays was 2.4%. This number was obtained by estimating the efficiency with a high-statistics MC simulation, then correcting that estimate for event losses during hand scanning and effects that were not simulated in the MC. The hand-scanning efficiency was measured to be 0.91, as described in Sec. IX A. The primary effects that were not simulated properly by the MC were electronic cross talk and charge migration from one drift cell to its neighbors. Initially, the correction for MC deficiencies was estimated to be 0.85 from a study of many real and MC events with the single-event display. Subsequently, this correction was measured to be 0.84 during the π^0 -decay studies (Sec. VIII E).

The overall efficiency of the photon spectrometer may be understood as follows. The ideal upper limit for the efficiency was 5.5%. This was determined by simulating 52.8 MeV photons from $\mu \rightarrow e\gamma$ decays with the MC assuming all detector channels were perfectly efficient, selecting those events that passed the hardware first- and second-stage triggers, then analyzing them using the actual space points from the e^+ and e^- trajectories recorded in the MC history files.

This estimate neglected event losses due to finite detector efficiencies and realistic pattern recognition, in addition to those mentioned above. The correction for finite detector efficiency was 0.91. It included comparable contributions due to the scintillators and the delay-line drift chambers, and smaller contributions due to the MWPCs and the other drift chambers.

The expected correction for pattern recognition losses was estimated to be 0.70. Here 25% of the events contained additional hits in the vicinity of the vertex or an edge from subsequent e^+ or e^- loops that made it impossible to identify the initial e^+ and e^- tracks uniquely. In practice, approximately half of these events reconstructed properly nonetheless. However, the remaining events often had fitted energies well above the true photon energies. Therefore, all such events were rejected to obtain a significant reduction in background at the expense of a modest loss of efficiency. Here 7% of the events consisted of e^+e^- pairs with highly asymmetric energy sharing that could be reconstructed using the MC space points, but not from the drift chamber information alone. For these events, the track of the low energy particle included four space points in the MC history file, but one or two of the corresponding drift distance measurements were obscured by hits from the high energy particle on the same cell. Combining these effects, the expected efficiency of the photon spectrometer was 2.7%. The 10% deviation from the true efficiency was caused by the remaining inadequacies in the pattern recognition and reconstruction codes.

VII. POSITRON EVENT RECONSTRUCTION

A. On-line pattern recognition

An analytic reconstruction code (ARC) was used in the on-line filter to determine the search region in the positron MWPCs and scintillators for hits that supported a $\mu \rightarrow e\gamma$ hypothesis. The code used the coordinates $(R_\gamma, \phi_\gamma, z_\gamma)$ and time, T_γ , from the on-line photon pattern recognition code to examine a limited range of positron scintillators. These scintillator ranges were established by systematic MC studies of $\mu \rightarrow e\gamma$ candidate events and set to include all positron candidates for a given $(R_\gamma, \phi_\gamma, z_\gamma)$. If no hit positron scintillators were found within 32 ns following the photon trigger, the event was abandoned. Adjacent positron scintillators within the range with TDC times within 2 ns were assumed to be associated with the same positron.

For a selected hit scintillator in the range, a triple coincidence in Snow White, consisting of a hit anode and an overlapping pair of stereo cathodes, was demanded within an azimuthal window adjacent to the hit scintillator. This triple coincidence indicated the passage of a positron through Snow White into the scintillator. If no triple coincidence was present, the scintillator was not used and the next scintillator in the range was examined. If a triple coincidence was found, it was assumed to provide a space point (x_{sw}, y_{sw}, z_{sw}) along the $\mu \rightarrow e\gamma$ positron orbit, and the scintillator provided the orbit end time, T_e , from calibrated TDC information. (The time T_e was corrected for light propagation along the scintillator.)

The photon and positron information were used to obtain an analytical estimate of the path of a $\mu \rightarrow e\gamma$ positron through the positron spectrometer. (The details of this orbit calculation can be found in Appendix B.) In the calculation, the positron was *assumed* to originate from a $\mu \rightarrow e\gamma$ decay at rest in the slanted target. The positron emerged with a momentum \mathbf{p}_e (52.8 MeV/c) directed opposite to the momentum of the trigger photon \mathbf{p}_γ (52.8 MeV/c). The estimated positron helical track was then projected through its intersections with the positron MWPCs where anode-cathode triple coincidences were expected. Using MC generated $\mu \rightarrow e\gamma$ decays, windows were established around the calculated positron trajectory. The size of these windows was tuned to optimize the acceptance for the $\mu \rightarrow e\gamma$ signal while rejecting photon triggers with no $\mu \rightarrow e\gamma$ positron present (background).

If the number of missing triple coincidences in the windows along the positron track did not exceed an established maximum, the event was written to tape as a $\mu \rightarrow e\gamma$ candidate. If, however, the number of missed triple coincidences exceeded this limit, the hit scintillator was not used and the process was repeated for the next hit scintillator in the possible range. If the event was not kept after all hit scintillators in the range were examined, the entire process was repeated with the value of T_e adjusted by ± 2 ns to allow for possible on-line timing misalignments. During the 1994 and 1995 run periods, the value of T_e was also adjusted by ± 4 ns if necessary, and the event checks repeated. The increased search provided a better measure of the background time spectrum in the vicinity of the $\mu \rightarrow e\gamma$ signal region.

The performance of the ARC filter was benchmarked on MC signal events, generated assuming design chamber efficiencies, overlaid either on real data or on simulated backgrounds. With this overlay, the success rate could be measured at the full intensity of the beam. The filter found 89% of the $\mu \rightarrow e\gamma$ events within the nominal geometric acceptance, while passing no more than 0.1% of the background. The selection reduced the number of taped events by approximately two orders of magnitude. This pass rate was much less than the 15% quoted in Sec. III H because less stringent criteria (e.g., broader windows, fewer hits) were ultimately required to define an event as acceptable in the on-line filter. The 11% loss in signal acceptance was due in large part to losses associated with anode and cathode inefficiencies. An additional small loss was attributed to failures in the iterative calculation of the orbit in cases where the positron orbit was nearly parallel to the planar target at the muon decay point.

B. Off-line event reconstruction

Two closely related reconstruction codes were employed in the off-line analysis of the positron data [23]. The first applied when the rates were low, and attempted to find all tracks in the event. This approach was not feasible in the high rate environment during data acquisition. Thus the second algorithm was confined to a search in the phase space where a candidate track had some reasonable probability of being a $\mu \rightarrow e\gamma$ event. The two programs had many features

in common, but the special treatment of high rates is noted below. Unlike the photon reconstruction program, this code was challenged to find real events that at high rates were not easily visualized.

The logic of the reconstruction was to define the clusters of electronically struck wires induced by the positrons as they crossed the chambers, and these clusters were grouped into potential space points. Disregarding the non-uniformities in the magnetic field, a good track swept out a helix as the positron propagated from its decay point to the scintillators. The space points defined above projected to a circle when observed in an end view, and formed a straight line when unrolled in a coordinate system consisting of the longitudinal position and the turning angle measured from the decay point. Hence, the algorithm looked for circles amongst the candidate space points, and used these circles to search for the full three-dimensional track. At high rates, tracks made from uncorrelated hits, “ghost” tracks, were reasonably probable, so that stringent quality criteria were required to ensure, with good probability, that tracks were real. A summary of the techniques used to construct the space points and, ultimately, the tracks is given in Appendix C.

The track reconstruction algorithm described in Appendix C ignored the impact of energy loss and multiple scattering in the fitting process. Hence, the resolution was not optimal and the computed energy was the average of the positron energy at the two ends of the track. A final least-squares fit was done to include these effects. Hits from a track were fit to calculated trajectories propagated through the detector system. Good tracks were required to have a χ^2 per degree of freedom below 3.0. The parameters were the position and momentum components of the positron at the first chamber crossing after leaving the target. Later, the final fit track was stepped back to the target to get the properties of the decay. During propagation, the mean energy loss in each material was subtracted from the energy of the particle. Hence, at the decay point, the fit was a good approximation to the decay energy. Multiple scattering was taken into account in the design matrix [24] (the inverse of the weight matrix). Contributions to the position resolution of the predicted hits were found numerically and added in quadrature with the intrinsic resolution of the chamber hits. As a given anode wire could be hit several times by a positron, the resolution of these wires was summed over all the loops. Thus a single anode wire was fit only once and had a single weight for all loops.

C. Performance

The best measure of the performance of the track reconstruction and fitting algorithms is the positron energy spectrum described in Sec. VIII A. The three features to note are the absolute energy of the kinematic threshold, the width of the edge, and the existence of unphysical events above the cutoff. A typical low-rate muon-decay spectrum is shown in Fig. 7. The central energy of the edge is 52.21 MeV, the resolution is 188 keV rms, and there is very little high-energy tail. The value of the central energy is about 0.6 MeV below $m_\mu/2$ because the fit momenta were not corrected for energy loss. The resolution is much closer to the MC simulation,

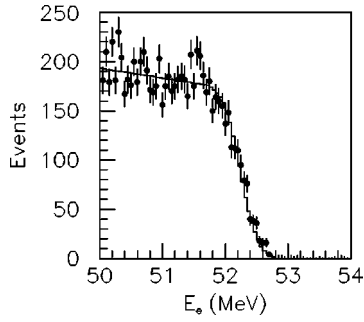


FIG. 7. The E_e spectrum from $\mu^+ \rightarrow e^+ \nu \bar{\nu}$ extracted from low-rate data. The solid curve is the fit used to extract the energy and resolution of the edge.

which predicts 161 keV rms, than the high-rate data because the space points are less confused with the overlapping hits in the chambers; the residual difference between MC and data is due to cross talk in the electronics.

The positron energy spectrum observed at full rate is displayed in Fig. 8. The absolute energy is within 10 keV of $m_\mu/2$, indicating that the mean energy loss was properly calculated in the final fit. The energy resolution is 230 keV σ at 52.83 MeV. The resolution must be compared to the MC simulation of the positron line shape from the $\mu \rightarrow e \gamma$ process. For low rate data this value is 180 keV for events with the same “topology,” i.e. the same number of loops and chambers traversed. When these simulated events were overlaid onto a background of high rate events, the resolution degraded to 210 keV. This value is in reasonable agreement with data, given the inadequacies of the simulation with respect to noise in the detector. About 3% of the events are above the kinematic cutoff. These events are unphysical, and are composed of fragments of different tracks that fooled the reconstruction algorithm. They cause a minor reduction in the efficiency for detecting $\mu \rightarrow e \gamma$.

The efficiency of the track finder was rate dependent. As discussed in Sec. VIII A, the low-rate efficiency of the track finder was 65%. As the rate increased to the operational intensity of 250 MHz (instantaneous), another 23.5% of the events were lost. The linear dependence of the efficiency of the track finder on rate is illustrated in Fig. 9. This plot was created by taking a set of reconstructed positron tracks from

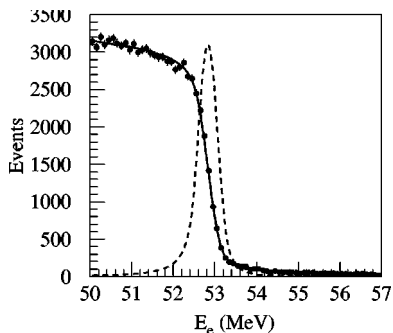


FIG. 8. The E_e spectrum from $\mu^+ \rightarrow e^+ \nu \bar{\nu}$ extracted from full rate data. The solid curve is the fit used to extract the line shape (dashed curve).

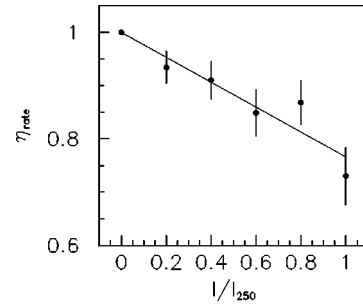


FIG. 9. The rate dependence of the efficiency of the reconstruction code. The relative efficiency, η_{rate} , is defined to have a value of 1 at low muon-stopping rates. The relative rate is defined as the ratio of the instantaneous beam intensity, I , to an instantaneous intensity of 250 MHz, I_{250} .

normal muon decay, selecting those above 50 MeV, and overlaying them onto real background events of varying rates. If the same events were found with the same energy and position properties to within 2σ , the events were considered to be properly reconstructed in the high rate environment. A similar result was found by overlaying simulated events on the real background.

VIII. SUPPLEMENTARY MEASUREMENTS

A number of supplementary measurements were performed during the experiment. Several utilized dedicated data sets that were taken under special conditions in order to test the energy, timing and tracking resolutions of the positron and photon spectrometers, and the ability of the MC codes to simulate these resolutions reliably. In addition, various subsets of the $\mu \rightarrow e \gamma$ production data events were used to improve the time resolution of the spectrometers and to optimize the global timing offsets between the positron and photon spectrometers.

A. Normal muon-decay studies

Data were taken at a low instantaneous muon stopping rate (~ 500 kHz) using a positron scintillator as a singles trigger to calibrate the channel-by-channel efficiency and the energy response in the positron MC code. Additional data were taken to validate the MC simulation of the detector acceptance, as described below.

To determine the channel-by-channel efficiencies, the low-rate version of the reconstruction code was used to fit tracks to all available hits except at the crossing studied. The anode wire efficiencies were measured using 0-loop events (the loop number denotes the number of complete circles that a positron made through the spectrometer before hitting a scintillator), because multiple-loop events generated additional ionization, which increased the efficiency. The cathode efficiencies were determined from 1-loop, multiple-dwarf events, which were the least contaminated. The optimum size of the window, which was used to determine the presence of a hit, was 7 (5) anodes (cathode strips) wide.

The measured efficiency of a given channel was averaged over the length of an anode wire or a cathode strip. Typically

there were significant variations along the length of a wire or strip. For example, the efficiency was very low in the vicinity of the garlands. Each anode wire that was not connected to the high voltage created a “dead spot” on each cathode it crossed. Also, non-uniform gaps (due to deformed cathode foils [11]) created different gains in some parts of the chambers. These factors made the measured efficiency sensitive to the population of tracks along the wire or strip.

These measured efficiencies were used to generate an initial set of channel-by-channel effective thresholds, that was then read into the MC code. Using these effective thresholds, a set of MC events was generated and analyzed to determine the channel-by-channel efficiencies. When these efficiencies from the MC code were compared to those from the data, there were significant differences due primarily to differences in the populations of events. However, from the differences, a correction to the thresholds could be calculated and a new set of MC events was generated. The modified thresholds altered the population of events to bring them into closer agreement with events reconstructed from the data. After a few iterations (usually three) the agreement between data and MC simulation was better than 1% for most regions of the chambers. The effective thresholds used in the MC simulation allowed the modeling of single track efficiencies on an individual channel-by-channel basis. These efficiencies were in good agreement with measured data.

Several other comparisons between the low-rate data and MC simulation confirmed that the MC code correctly simulated the geometric and kinematic acceptance of the detector. These included matching the energy distribution of positrons for 0, 1, 2, and 3 loop events, and the loop-number distributions for all events and for events with positron energies above 45 MeV.

Data taken at low rates with a 0.25 mm thick vertical target were used to calibrate the absolute energy scale for positrons. This was accomplished by fitting the edge of the muon-decay spectrum separately for groups of events that made 0, 1, or 2 loops and were traveling either upstream or downstream. The six values for the edge energy were compared to values from the MC code, including the effects of energy loss in the target and detectors. Then a scale factor of 1.0096 was applied to the magnetic field map to match the data to the MC simulation; this achieved a precision of 10 keV in the absolute energy scale.

B. “Hole target” data

A good test of the positron pattern-recognition algorithm was the analysis of data taken at low stopping rate with a “hole target.” An elliptical target with a 2 cm \times 10 cm rectangular hole replaced the normal target positioned at the center of the MEGA detector. Reconstructed muon-decay positron tracks measured the known edges of the hole and determined the fraction of (incorrectly) reconstructed tracks that appeared inside the target hole.

Figure 10 shows a comparison of the observed intersections of data and MC positron helices with the target plane in a reference frame aligned with the plane of the target. The edges of the hole are clearly evident in the projection and the

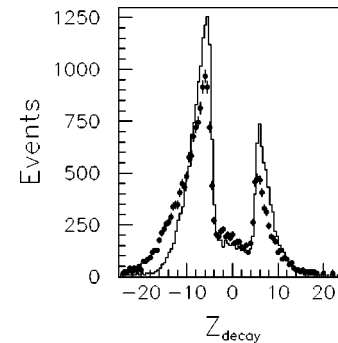


FIG. 10. Target intersection coordinates of low-rate muon-decay events when the coordinate in the perpendicular direction fell in the range of the hole in the target. The points represent measured events, and the curve represents an MC simulation.

agreement between data and MC simulation confirms that the position resolution is properly simulated. The differences in the overall shape of the projections are due to the use of a Gaussian shaped beam for the MC simulation that did not match the shape of the actual beam.

Many of the events that reconstructed within the target hole intersected the target at a very shallow angle and thus had poor position resolution in the plane of the target. Also, some events intersected the target at two points during their first loop. For these events, both intersections were kept even if one fell in the hole. The total fraction of events lying inside the hole was 4.9% in the data and 3.3% in the MC simulation. The difference resulted mostly from MC inadequacies in modeling the positron chamber efficiencies and detector noise. The discrepancy was larger for multi-loop events, which had a higher probability of passing near a garland. Likewise, detector noise produced extra chamber hits that degraded the spatial resolution and caused pattern-recognition failures.

The resolution of the positron-target intersection, as well as the resolution of the positron’s initial direction and energy, were degraded somewhat at higher stopping rates. These rate-dependent effects were modeled reasonably well by overlaying simulated high energy positron tracks on background events of real data taken at high rates, as described in Sec. VII C.

C. Off-line $e\text{-}\gamma$ timing

1. Timing within the photon spectrometer

The photon scintillators served the dual purpose of providing fast timing information to the trigger and photon timing relative to the positron. Dual-threshold discriminator circuits were used, instead of constant fraction discriminators, since the scintillators were subject to multiple hits from conversion pairs. The discriminators produced timing signals that had a pulse-height dependent slewing; to obtain the optimum timing resolution, it was necessary to correct for this.

On-line calibration of the photon scintillators relative to the ring counters was discussed in Sec. V F. Calibration constants were updated continuously during the data acquisition. However, on-line calibration did not include any correction

for pulse height. Also, background in the histograms degraded the resolution. As part of the off-line analysis, codes were developed to correct for pulse-height slewing and to improve the time resolution using MEGA data. In Sec. VI, the photon reconstruction algorithms were discussed. Timing corrections were performed using scintillator information obtained from the first-pass scintillators for events where both members of the conversion pair had well isolated “3-side” edges (see Appendix A). During the filter process, timing information for reconstructed photons satisfying this criterion was written to an output data stream and then processed with a separate timing analysis code.

The first-crossing arrival time of the e^+ and e^- at their scintillators should be the same when corrected for the flight time from the vertex. This flight time was calculated in the off-line filter code as part of the information determined from the circle fits. This time difference was not the same if pulse-height slewing caused a shift in one or both outputs, or if timing jitter appeared due to background problems. Data from successive calibration runs were used to obtain correction factors for these two effects.

The procedure used to obtain the timing correction factors began by determining the apparent time difference between the two edges of the events. Fits to the time difference spectra were used to produce an $N_{scint} \times N_{scint}$ matrix of time differences for each layer. In order to determine the coefficients needed to minimize the time jitter, the matrix was inverted subject to the constraint that the off-line timing correction factors averaged to zero within each photon layer. Using these corrections, the data were replayed to obtain, event by event, the time at each end of a scintillator after correcting for the time of flight along the scintillator. A fit was made to this arrival time versus pulse height for each photomultiplier tube to obtain a pulse-height slewing correction. A final pass through the data allowed the pulse-height correction constants to be applied to the time differences, and then the time offset corrections were recalculated. Following this procedure the photon scintillator timing was improved by a factor of ~ 1.8 relative to the on-line timing resolution. These pulse-height slewing and alignment timing constants were then used in the final event analysis.

2. Timing within the positron spectrometer

The positron spectrometer scintillators also needed to be timed with respect to each other and corrected for pulse-height dependent slewing. As with the photon spectrometer, the scintillators in the positron spectrometer were timed with respect to each other by calculating time differences between scintillators that should be in time, plotting these time differences versus the pulse height in the scintillator, and forcing the average time difference to be zero. The same mathematical methods were used in both spectrometers, but the data selection was somewhat different. In the positron spectrometer, data from positron scintillator clusters were collected, and the time differences between adjacent scintillators, the charges on the scintillators, the z position of the hit on the scintillator, and the information of whether the cluster came from an even or odd event were stored. The z positions of the scintillator hits were used to correct the scintillator times for

the transit time in the scintillator. Slewing corrections and time offsets were then calculated for all upstream and downstream phototubes, for both even and odd events.

3. Timing between the photon and positron detectors

Section V F describes the routine timing calibrations that were performed over the course of the experiment, and the previous subsections describe the improvements to these timing constants that were obtained during the off-line data analysis. However, while the off-line timing constants significantly improved the overall time resolution, they were derived “locally,” within a given photon layer or group of positron scintillators, so they did not ensure that the timing offsets were optimized between the two spectrometers. This match was achieved by studying production data events that contained coincident hits in a ring counter and a positron scintillator, together with a high-energy photon shower.

During the off-line event filtering (see Sec. IX A), those events that contained a fully reconstructed high-energy photon and a ring counter hit were selected for further analysis if the photon propagation direction projected back to the vicinity of the ring counter and the time difference between the high-energy photon and the ring counter hit satisfied a loose coincidence constraint.

These events were then subjected to several additional cuts to isolate those with coincidences between a positron scintillator cluster (one or more contiguous positron scintillators in time coincidence with each other) and the high-energy photon shower. These cuts included the following: (1) the z location of the photon conversion must be consistent with the ring counter and photon layer that were hit, (2) the positron scintillator cluster must be in time coincidence with the ring counter, and (3) the ϕ coordinate of the positron scintillator cluster must be consistent with both the ϕ location of the high-energy photon shower and the ϕ location of the ring counter hit. Also there must be no more than one additional positron scintillator cluster within a ± 15 ns time window and a ± 1 rad angular window in ϕ about the time and location of the high-energy photon shower on the same end of the positron spectrometer as the hit in the ring counter. Furthermore, if a second positron scintillator cluster was present, it must be out of time with respect to the ring counter hit.

For each event that passed all these cuts, the difference between the time of the positron scintillator cluster hit and the high-energy photon shower, corrected for the different propagation distances of the positron and the photon, was calculated. Time differences were saved in 12 histograms—keyed by photon spectrometer layer 1, 2, or 3, positron spectrometer upstream or downstream, and positron scintillator even or odd read out—for contiguous groups of data runs that were taken under similar conditions. Figure 11 shows time difference spectra for coincidences between the downstream, even positron scintillator TDCs and photon spectrometer layer 2 for two different groups of $\mu \rightarrow e \gamma$ data runs that were taken during 1994. The two groups have very different statistics because code was installed in the on-line filter to enrich the data sample of ring counter, high-energy photon coincidence events during the middle of the 1994

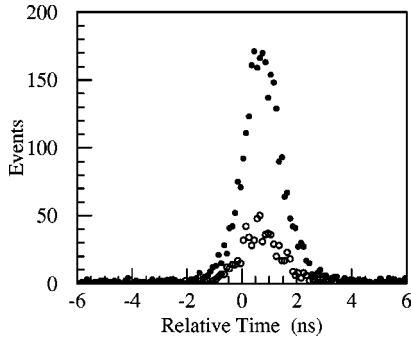


FIG. 11. Time difference spectra between positron scintillator clusters from downstream, even TDCs and high-energy photon showers in layer 2 for events that contained coincident ring counter hits. The open circles show the distribution for a group of 204 runs that were taken early in 1994, before the on-line filter code was modified to enrich the sample of ring counter, high-energy photon events. The solid circles show the distribution for a group of 211 runs that were taken later in 1994, after the on-line filter code had been modified.

data acquisition. This code saved all high-energy photon events to tape that appeared to originate in the vicinity of a struck ring counter when propagated back to the z axis. This was independent of whether or not the events also passed the on-line $\mu \rightarrow e\gamma$ event filter requirements.

The 12 histograms for each group of runs determined the 12 global timing offsets needed to align measurements in the positron and photon spectrometers. All of the final offset corrections were found to be less than 1.2 ns, which implies that the timing calibration constants used during the on-line and preliminary off-line filtering were sufficient to ensure good efficiency for acceptance of any true $\mu \rightarrow e\gamma$ events. The measured offsets were also quite stable over the duration of each run period. In principle, the 12 global timing offsets could be reduced to 6 linearly independent time differences. Attempts to do so, however, found non-statistical effects at the level of ~ 0.1 ns that were attributed to small electronic propagation time differences through (nominally identical) parallel circuit paths within the routing box and data acquisition gating circuitry. Therefore, the 12 separate offsets were used without modification during the final stages of off-line analysis.

D. $\mu \rightarrow e\gamma\nu\bar{\nu}$ studies

Observation of the IB process $\mu \rightarrow e\gamma\nu\bar{\nu}$ demonstrates that the apparatus could detect coincident $e-\gamma$ events. At nominal beam intensity, this process was completely engulfed by random coincidences. Figure 12 shows the $t_{e\gamma}$ spectrum for IB events using the standard first- and second-stage hardware triggers, but with the beam intensity reduced by a factor of 60, the magnetic field lowered by 25%, and the $\mu \rightarrow e\gamma$ on-line filter suppressed. The peak shown is for all energies of the detected decay products. The area of the peak is very sensitive to the exact acceptances of the detector at its thresholds, and was calculated by MC simulation to better than a factor of 2. If the data and the simulation are restricted to $E_{\gamma} > 46$ MeV, $E_e > 40$ MeV, and $\theta_{e\gamma} > 120^\circ$, the branch-

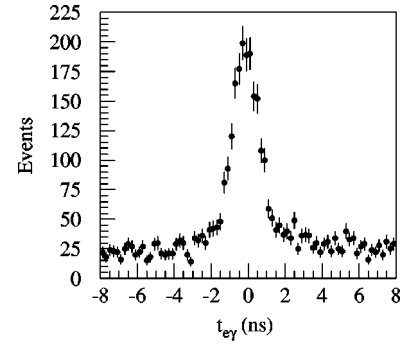


FIG. 12. Values for $t_{e\gamma}$ from the process $\mu^+ \rightarrow e^+ \gamma \nu \bar{\nu}$ under the conditions of reduced rate and magnetic field.

ing ratio is reproduced within 20%. The uncertainties in the IB normalization do not affect the precision of the $\mu \rightarrow e\gamma$ acceptance, however, because the IB preferentially occurs near the energy-cut boundaries while the $\mu \rightarrow e\gamma$ process occurs well above these cuts.

The shape of the timing peak is characterized by a Gaussian with 0.77 ns rms. The dominant contributor to the width is the photon timing, as measured in a stopping-pion experiment, which must be scaled down from about 70 to 40 MeV for comparison. At 52.8 MeV, the MC simulation indicated that the photon-positron resolution was 0.68 ns rms.

In the IB and $\mu \rightarrow e\gamma$ processes, the origin of the photon is defined to be the intersection of the positron track with the target. The photon trace-back angle, $\Delta\theta_z$, specifies the difference between the polar angles of the photon as determined from the lines connecting the decay point to the photon conversion point and the direction of the reconstructed e^+e^- pair. The resolution of $\Delta\theta_z$ is dominated by multiple scattering of the pair in the lead converters. The observed response for inner and outer conversion layers of the IB process is in excellent agreement with the MC simulation, as seen in Fig. 13. The trace-back resolutions appropriate for the $\mu \rightarrow e\gamma$ analysis are 0.067 and 0.116 rad rms for conversions in the outer and the inner lead layers, respectively.

E. π^0 decay studies

The energy resolution of the photon spectrometer was measured by observing the reaction $\pi^- p \rightarrow \pi^0 n, \pi^0 \rightarrow \gamma\gamma$. When the π^- is captured at rest and the two photons from the π^0 decay are back to back, the energies of the photons are 54.92 and 82.96 MeV. Since the 54.92 MeV photon is very close in energy to the 52.8 MeV photon from $\mu \rightarrow e\gamma$ decay, it was used to determine the energy resolution of the spectrometer at 52.8 MeV. At full intensity, the stopping π^- rate was approximately a factor of 40 smaller than the stopping μ rate in normal data taking. However, the π^- trigger rates (see Table III), which directly depend on the number of γ 's observed in the photon detector, were a factor of 2 higher. Nonetheless, the total rate in the photon detector was small due to the magnetic shielding, and it is expected that the photon energy response function, as fit to this calibration, can be applied without change in the likelihood analysis described in a later section.

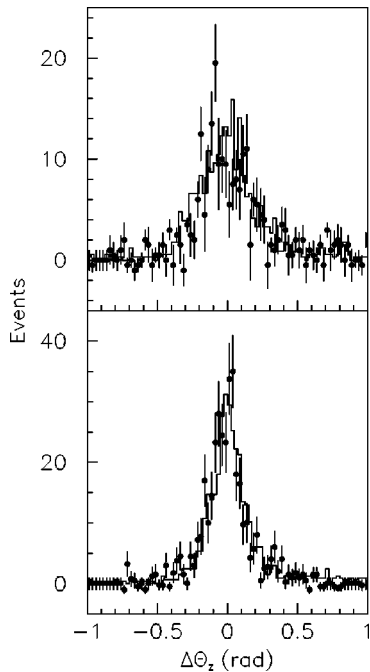


FIG. 13. The upper (lower) panel is the photon traceback resolution $\Delta\theta_z$ for the inner (outer) conversions obtained from IB events where both the muon decay and photon conversion points were known. Accidental coincidences have been subtracted.

The π^- were stopped in a CH_2 target and events with a potential $\pi^0 \rightarrow \gamma\gamma$ pair in the spectrometer were collected by triggering on events that had approximately back-to-back high-energy photon first-level triggers in two different spectrometer layers. These events were then analyzed by a filter that did a quick reconstruction of events and kept only those that had at least one photon that reconstructed with an energy between 76 and 96 MeV. These events were then analyzed by the full reconstruction code and the opening angle of the two photons and the reconstructed energies recorded. The expected energies of the two photons were also calculated from the opening angle of the photons and those energies recorded. The energy resolution was determined by plotting the difference between the measured energy and the calculated energy based on the opening angle, after an opening angle cut was placed on the events. For inner conversion layer events, the cut was $\theta_{\gamma\gamma} > 171^\circ$, and for outer conversion layer events, it was $\theta_{\gamma\gamma} > 173.5^\circ$. The cuts were selected to minimize resolution degradation due to uncertainties in the opening angle, but still retain enough events to determine the response functions accurately. For each set of events, the error in the calculated energy that came from the finite opening angle resolution was small compared to the resolution of the measured photon energy.

The energy resolutions that were obtained, for inner and outer conversion layer events, are shown in Figs. 14 and 15, respectively, where the measured energies have been shifted down by 2.1 MeV so the peaks may be compared to the simulated $\mu \rightarrow e\gamma$ decay signal. As can be seen, the energy resolution for inner conversion layer events is significantly worse than the resolution for outer conversion events. Degradation occurs because the e^+e^- pairs from inner conver-

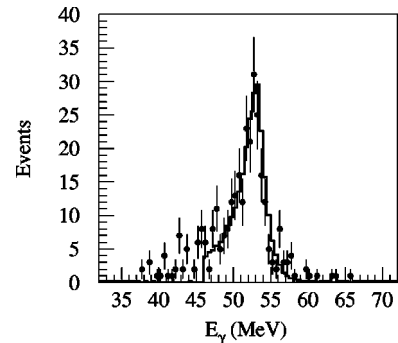


FIG. 14. The energy resolution of reconstructed photons from pion decay for events that converted in the inner conversion layer. The points come from data and the solid line shows reconstructed MC events.

sion layer events suffered significant multiple scattering and energy loss in the outer lead conversion layer before they were tracked by the drift chambers. The central energy and width of the distributions were well reproduced by the MC code. The differences in the low-energy tails were due to charge exchange of in-flight pions from carbon in the CH_2 target. The additional high-energy tails in the data were associated with contributions from other opening angles, due to special difficulties identifying the conversion point for the 83.0 MeV photon. The energy resolutions were 5.7% and 3.3% (FWHM) at 52.8 MeV for conversions in the inner and outer lead layers, respectively.

The timing resolution of the photon spectrometer was determined by looking at the time difference between the two photons in pion events. The resolution from the time difference of the two photons was divided by $\sqrt{2}$ and resulted in a timing resolution of 0.57 ns rms for single photons.

Finally, reconstruction inefficiencies caused by electronic problems that were not modeled in the MC simulation were studied with the pion data. Data events were selected that included a reconstructed high-energy (82.96 MeV) photon, and had an angular difference of $> 150^\circ$ between the high energy photon and the center of the shower of the second photon that triggered the event. MC pion events were generated and passed through the pion trigger software with the

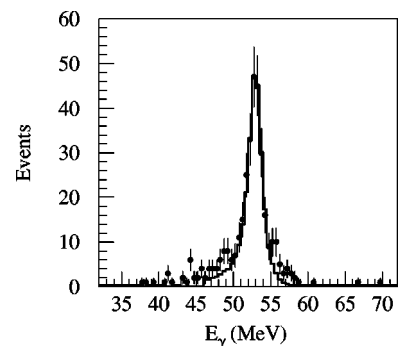


FIG. 15. The energy resolution of reconstructed photons from pion decay for events that converted in the outer conversion layer. The points come from data and the solid line shows reconstructed MC events.

same analysis cuts applied. The number of events that included a second reconstructed photon in the data set was compared to the number of photons reconstructed in the MC code, yielding a correction factor of 0.84, which was applied to calculated MC reconstruction efficiencies.

IX. DATA ANALYSIS

A. Event selection

The data recorded on line, 4.5×10^8 stored events, were passed through a set of computer programs that reconstructed all events that the pattern recognition algorithms could interpret. The analysis began by matching a run to constants that had been collected in run-number-keyed database files. These files included pedestals and timing calibration constants created during the data acquisition. The constants were used to convert raw information from the electronics into physical quantities. A separate set of files contained the geometry of the apparatus. Analysis of a subset of the data was used to produce a list of dead wires in the positron chambers.

The next step was to carry out the photon reconstruction, because this program was much faster than the positron reconstruction. Roughly 8% of the original sample passed energy and quality cuts in this part of the code. Next the positrons were analyzed. About 30% of the events that passed the photon cuts could be reconstructed. Very loose kinematic cuts were placed on these events. This left 0.15% (6.7×10^5) of the original events that were output to data summary tapes.

The above process took roughly one year of computing on a farm (20 processors) of UNIX workstations. These workstations were controlled by cshell scripts whose purpose was to find a run of data that had not been analyzed and make the run available to the processor. The scripts reduced the processing to keeping the disks filled with unprocessed data and checking the quality of the results. Pass rates and histograms corresponding to 40 different data distributions were monitored once per tape.

In the final analysis of the remaining events, the tracking code stepped the positrons through the magnetic field to get the best position and momentum vector at the target. Improved timing constants described in Sec. VIII C were also incorporated at this time. The results were added to the data stream and new data summary tapes were produced. Additionally, PAW ntuples [25] for 60 variables were retained. These ntuples were useful for obtaining high statistics distributions of random, uncorrelated backgrounds that were needed for the likelihood analysis.

With the final kinematics calculated for each event, the data set was further reduced to 5.5×10^3 events that were fully reconstructed and of continued interest. These events were required to have good-quality positron reconstructions, to satisfy separate χ^2_ν cuts on the positron and photon fits, and to pass loose cuts on the signal kinematics [$E_e > 50$ MeV, $E_\gamma > 46$ MeV, $|t_{e\gamma}| < 4$ ns, $\cos(\theta_{e\gamma}) < -0.9962$, and $|\Delta\theta_z| < 0.5$ rad]. Events in which the positron momentum vector at the decay point appeared to lie within 5° of the plane of the target were discarded.

To remove incorrectly reconstructed photon events, the images of the showers in the pair spectrometers were manually scanned. During the hand-scanning process, events were checked for clean edges and an unambiguous vertex, and those that showed clear contamination due to extraneous hits were rejected. Also events were rejected if the reconstruction of the first pass circle through the drift chambers was ambiguous or judged to be wrong. The efficiency for real photons was monitored by mixing about 500 MC 52.8 MeV photon events into the sample in a non-identifiable way and finding that 91% of the MC events passed, whereas only 73% of the data events were selected. Most of the rejected data consisted of two overlapping low-energy photon showers that had been reconstructed by the analysis program as a single high-energy shower. A small fraction of the rejected data had either edge or vertex contamination due to random background hits, primarily in the delay lines. Since random backgrounds, consistent with the measured rate at full beam intensity, were included in the MC generated events, some of the 9% that were rejected were due to edge and/or vertex contamination. The remaining MC events which were rejected were judged to have an incorrect reconstruction through the drift chambers. Note that no manual scanning of positron spectrometer events was performed. The remaining sample of 3971 data and 450 MC events was stored in an ntuple as the input to the likelihood analysis (Sec. IX D). This sample was large enough to allow a study of the background.

B. Normalization

Two quantities that are very important for the calculation of the $\mu \rightarrow e\gamma$ branching ratio are the acceptance of the detector and the number of muons stopped in the target. The number of stopped muons was determined by counting the number of decay positrons striking one of the scintillators in the upstream array of the positron scintillator detectors, as described in Sec. III B. The acceptance of the apparatus, which includes geometrical, trigger, and pattern recognition constraints, was obtained by simulating 1.2×10^7 unpolarized $\mu^+ \rightarrow e^+ \gamma$ decays for a 1993 data set that was then used as the standard run. Of the thrown MC events, 5.2×10^4 survived processing by the same codes used for the data analysis. Thus the probability for detection of a $\mu \rightarrow e\gamma$ decay was 4.3×10^{-3} . This value included a 9% reduction for the inefficiency of manual scanning of the photon reconstructions, as described in the previous section. An additional $20\% \pm 4\%$ reduction was made to account for inadequacies in the MC simulation that over-estimated the acceptance. The majority of this effect arose in the photon spectrometer, where both electronic cross talk and charge drift between neighboring drift chamber cells reduced the true detector acceptance, relative to that predicted by the MC simulation, as described in Sec. VI C. In addition to degrading the energy resolution as discussed in Sec. VII C, inter-channel cross talk in the positron spectrometer led to a small acceptance loss, which was estimated by comparing the images of many data and MC events.

Since the data were taken over a span of 3 years, the efficiencies of the detector underwent a number of changes. To account for this, run-by-run corrections were made to the stopped muon rate relative to the standard run. The nearly 4000 data runs were divided into several groups that reflected major changes in the detector performance such as an inoperative photon layer, an inoperative positron chamber, a change in the instantaneous beam rate, or a change in the noise level of the photon spectrometers. The largest change, up to 40%, occurred when a photon layer was inoperative. For the 1994 and 1995 data there was an additional 10%–15% loss in performance due to a reduced acceptance in the first drift chamber, DC1. This reduction occurred because the drift chamber threshold was lowered and led to increased inter-channel cross talk, which contaminated the vertex and edge of some events. The rate dependence of the positron reconstruction algorithm also led to a change in efficiency when the instantaneous beam rate changed. The majority of the data were taken at a beam rate within $\pm 12\%$ of the nominal 250 MHz. Fluctuations in the instantaneous beam rate resulted in a correction of approximately 2%–3%. The variation in the muon stopping rate had less than a 1% effect on the photon reconstruction efficiency and no corrections were made for it. The high instantaneous beam rate was also responsible for increased dead time in the detector and resulted in a loss of about 10% of the effective number of muons stopped in the target.

In addition to the corrections noted above, there were other run-by-run corrections of order 5% or less for changes such as modifications to the software used in data acquisition and analysis. After all of the above corrections were made, the estimated total number of muons stopped in the target during the 3 calendar years of data taking (8×10^6 s of live time) was $N_s = 1.2 \times 10^{14}$. After convoluting N_s with the acceptance, the single event sensitivity for the experiment was $2.3 \pm 0.2 \times 10^{-12} = 1/N_\mu$, where N_μ was the number of useful stopped muons.

C. Cut analysis

Before embarking on the complexities of a likelihood analysis, the result of a so-called blind box analysis is presented. In this method, cuts are placed around the signal region based on the width of the response functions. The width of the window was taken to be $\pm 2\sigma$ in each of the five parameters, $E_\gamma, E_e, t_{e\gamma}, \theta_{e\gamma}$ and $\Delta\theta_z$. As there were many subsets of the data for different types of events, it is imprecise to combine all the data together. Nevertheless, the results are plotted in Fig. 16 with the E_γ and E_e variables shown explicitly for inner and outer conversions. The box in each panel is where the signal would be found in the absence of background. Three events fall inside the boxes, but they appear consistent with the background. If one takes the three events inside the boxes as background, then the branching ratio limit is about 20% greater than the one obtained by the likelihood analysis below. The primary difference arises because each of the events is near the edge of the boxes and is improbable as real signal.

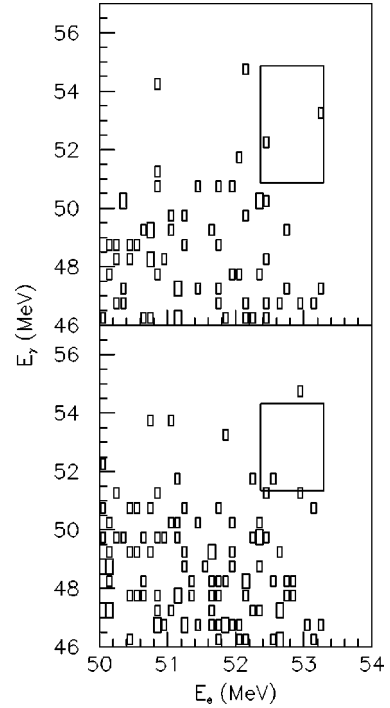


FIG. 16. A box analysis of the data. The upper (lower) panel shows the events from inner (outer) conversions plotted as a function of the photon and positron energies. The large rectangle in both panels is the $\mu \rightarrow e\gamma$ signal area for $\pm 2\sigma$ in the parameters shown.

D. Likelihood analysis

Each event has its own characteristics, e.g. inner or outer photon conversion and positron resolution group, with different resolutions in the five parameter space of kinematic parameters. The likelihood analysis provides a natural way to combine the data of different types of events by assigning the proper probabilities for signal and backgrounds. The likelihood analysis also uses all information known, either from the data, auxiliary measurements, or Monte Carlo simulations, to separate signal from background in a sound mathematical way. It determines whether events found in a given kinematic region should be interpreted as signal or background.

The five kinematic properties, in conjunction with the detector response, determined the likelihood that a $\mu^+ \rightarrow e^+ \gamma$ signal was detected. The determination of the detector acceptance and response functions relied on MC simulation to extrapolate from experimental input for measured responses to the kinematic region of the $\mu \rightarrow e\gamma$ signal. The determination of the number of $\mu \rightarrow e\gamma$ events in the sample was evaluated using the likelihood method described in the analysis of previous experiments [26]. The formula for the normalized likelihood is

$$\mathcal{L}(N_{e\gamma}, N_{IB}) = \left(1 - \frac{N_{e\gamma}}{N} - \frac{N_{IB}}{N} \right)^{N-m} \prod_{i=1}^m \left[\frac{N_{e\gamma}}{N} \left(\frac{P}{R} - 1 \right) + \frac{N_{IB}}{N} \left(\frac{Q}{R} - 1 \right) + 1 \right], \quad (2)$$

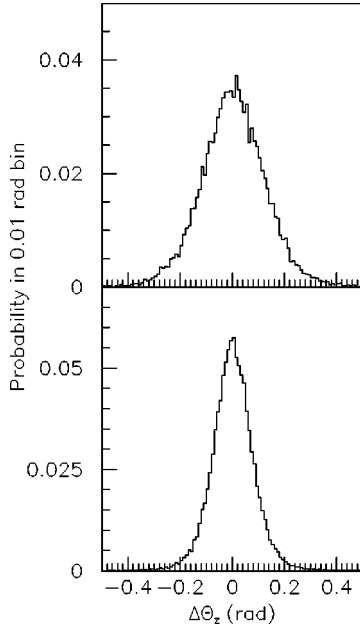


FIG. 17. The signal PDF for $\Delta\theta_z$ for inner (outer) conversions is shown in the upper (lower) panel, as generated by MC simulation.

where $N=3971$, $N_{e\gamma}$ is the number of signal events, N_{IB} is the number of IB events, and P, Q , and R are the probability density functions (PDF) for signal, IB, and randoms of each of the five parameters describing the event. The values of P, Q , and R depend on the type of event, and the likelihood analysis provides a natural mechanism for handling the independent topology of each event. The value of $m \leq N$ was chosen to speed the calculation and leave the value of the likelihood unchanged if $P/R \leq 0.01$ and $Q/R \leq 0.01$ for all events left out of the product. The value of m was 3832 for this experiment. The events fell into the following categories: positron topology, photon conversion plane, target intersection angle, and data collection period. As a result, PDFs were extracted for each class of events and applied according to the classification of individual events.

The PDFs P and R are the products of statistically independent PDFs for the five parameters, each normalized to unit probability over the full range of the variable for the sample. The signal distributions for the photon depended on whether the photon converted in the inner or outer lead converter in each pair spectrometer. The distributions for E_γ shown in Figs. 14 and 15 were derived from MC simulations that had the same input as those compared to the pion data in Sec. VIII E. The energy resolutions were 3.3% and 5.7% (FWHM) for conversions in the outer and inner lead layers, respectively. Likewise, the distributions for $\Delta\theta_z$ were derived from a MC simulation that had the same input as those compared to the IB data in Sec. VIII D. They are plotted in Fig. 17. The trace-back angular resolutions were 0.067 and 0.116 rad rms. These distributions were somewhat narrower than those measured from the IB in Fig. 13 because the photon energy is higher in the $\mu \rightarrow e\gamma$ process than in the IB. The distribution for $t_{e\gamma}$ was also based on the IB data and had a resolution of 0.68 ns rms as shown in Fig. 18. There was no way to measure the response function for $\cos(\theta_{e\gamma})$.

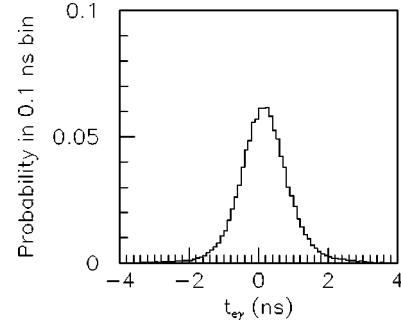


FIG. 18. The PDF for the timing variable associated with the $\mu \rightarrow e\gamma$ signal. This PDF was generated with MC that reproduced the experimental IB relative-time distribution, and had a slight dependence on the photon energy.

Thus the MC simulation was relied upon to produce this distribution and gave the average FWHM for $\cos(\theta_{e\gamma})$ as 1.21×10^{-3} at 180° . Given helical tracks, the location of the target was critical to obtaining the correct absolute value of $\cos(\theta_{e\gamma})$. The mechanical survey provided the most accurate measurement for the analysis. The resolution also depended on the angle the track made with the target, and some representative distributions are plotted as a function of target angle in Fig. 19. All of the above distributions were used directly in the likelihood analysis and came from high-statistics MC simulations.

Three types of positron topologies (i.e., number of dwarfs encountered and number of loops) were determined empirically.

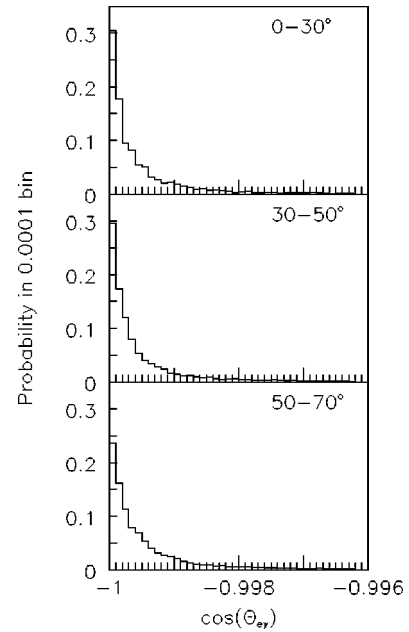


FIG. 19. The PDF function for the cosine of the angle between the positron and the gamma ray, as generated by MC simulation for the $\mu \rightarrow e\gamma$ signal. The panels are labeled by the angle between the target normal and the positron momentum unit vector at the target, which can range from 0 to 180° . The PDFs are slightly asymmetric about 90° because the target faced a dwarf on one side and faced the gap between dwarfs on the other side, which induced a small change in the precision of measuring the positron trajectory.

TABLE V. Representative fitting parameters for topology groups A and C for the last third of the 1995 data, one of the periods treated separately in the likelihood analysis.

	E_0 (MeV)	σ (MeV)
Group A	52.835(0.019)	0.218(0.009)
Group C	52.814(0.030)	0.391(0.018)
Group A MC	52.834(0.002)	0.161(0.001)
Group C MC	52.826(0.003)	0.270(0.003)

cally from the 1993 data to obtain three statistically equivalent size samples. When extended to all the data, the groups maintained their resolution characteristics. For the three types of positron topologies, the signal was extracted by fitting the positron edge in the following way. The function

$$\mathcal{F}(E) = \begin{cases} \frac{C_L}{(E_0 - E)^{2.05}} & \text{if } E < E_0 - \sqrt{2.05}\sigma, \\ ae^{-((E - E_0)/\sqrt{2}\sigma)^2} & \text{if } E_0 - \sqrt{2.05}\sigma \leq E \leq E_0 + \sqrt{3}\sigma, \\ \frac{C_U}{(E - E_0)^3} & \text{if } E_0 + \sqrt{3}\sigma < E, \end{cases} \quad (3)$$

represented the positron monoenergetic line shape. The constants C_L , a , and C_U were related by the continuity condition at the region boundaries. The asymmetry in the non-Gaussian tails reflected the straggling present in the energy loss of the positrons. The function $\mathcal{F}(E)$ was convoluted with the function

$$\mathcal{G}(E_e - E_0) = \begin{cases} 1 + b(E_e - E_0) & \text{if } E_e \leq E_0, \\ c + d(E_e - E_0) & \text{if } E_0 < E_e, \end{cases} \quad (4)$$

and then fit to the spectrum. The terms involving $b-d$ were needed to accommodate the change in acceptance as a function of energy below E_0 and ghost events above E_0 . The parameters of the fit were $a-d$, E_0 , and σ . The values of the fit parameters were used in the likelihood analysis for events by topology group and run period. The results were quite stable as a function of run period. Some representative results for E_0 and σ for 1995 are shown in Table V. All the central energies agreed within errors to $m_\mu/2$. The patterns of resolutions between MC simulations and data agreed, but the data resolution was clearly degraded by problems with electronic noise in the detector that smeared the location of the space points. This was not modeled in the MC simulation. The experimental values for σ were used for the signal distributions in the likelihood analysis. The fits are displayed in Fig. 20, where the solid curves are the fits to the points and the dashed line is the parametrized line shape used for the $\mu \rightarrow e \gamma$ signal PDF. Figure 8 is a similar plot for group B data for all years.

The background PDFs were extracted from the spectral shapes of a much larger sample of events, where the other statistically independent parameters remained loosely con-

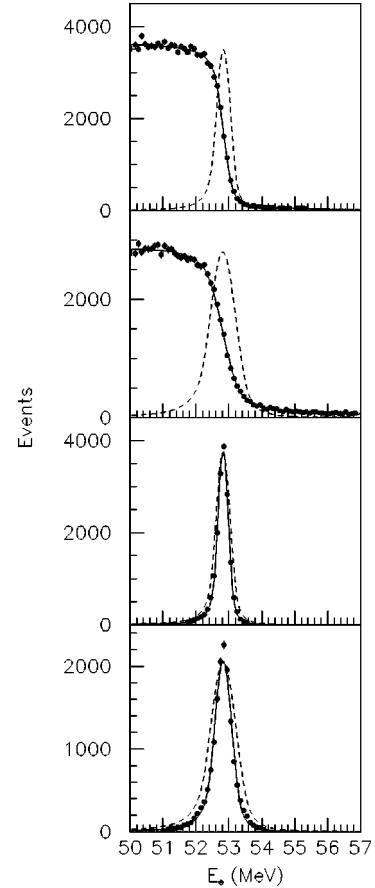


FIG. 20. Unnormalized PDFs for the positron energy distributions in correspondence to the cases described in Table V. The top two panels illustrate the data for the last part of 1995 for groups A and C. The solid lines are fits that are normalized to become the background PDFs. The dashed lines are the monoenergetic line shapes produced with the same parameters as the fit, and they are normalized to become the signal PDFs. The data points in the lower two panels are generated with MC simulations. The solid curves are fits to these line shapes used to extract the centroids and resolutions for the table. The dashed lines are the line shapes produced from the fits in the upper two panels; they illustrate the energy resolution degradation described in the text.

strained. The PDFs for the outer and inner photon conversions are shown in Fig. 21, where the shape was modified to account for the efficiency of the hand scanning. The correction functions used were

$$\begin{aligned} &0.77 && \text{if } E_\gamma \leq 51 \text{ MeV}, \\ &0.77 - 0.064(E_\gamma - 51) && \text{if } 51 \text{ MeV} < E_\gamma \leq 56 \text{ MeV}, \\ &0.45 && \text{if } 56 \text{ MeV} < E_\gamma, \end{aligned} \quad (5)$$

and

$$\begin{aligned} &0.71 && \text{if } E_\gamma \leq 51 \text{ MeV}, \\ &0.71 - 0.086(E_\gamma - 51) && \text{if } 51 \text{ MeV} < E_\gamma \leq 56 \text{ MeV}, \\ &0.28 && \text{if } 56 \text{ MeV} < E_\gamma, \end{aligned} \quad (6)$$

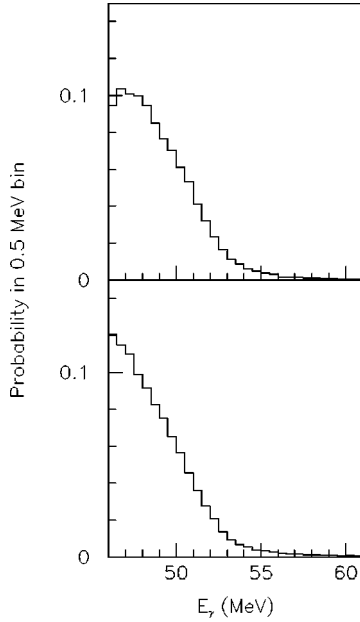


FIG. 21. The upper (lower) panel shows the energy PDF of the background gamma rays for the inner (outer) gamma ray conversions.

for outer and inner photon conversions, respectively. The error in Eqs. (5) and (6) was limited by the statistics of the sample of events that were manually scanned. Empirically, the likelihood function seemed moderately insensitive to the coefficients in these equations. A representative PDF for $\Delta\theta_z$ is shown in Fig. 22. The distribution was not very dependent on whether the conversion was from the inner or outer lead converters, but did have a mild dependence on the photon energy. This shape was largely determined by the beam stopping distribution. Although this distribution is peaked at $\Delta\theta_z=0$, it is still significantly broader than those in Fig. 17 and gave some useful discrimination between prompt and accidental processes. The PDFs for $t_{e\gamma}$ are shown in Fig. 23. They are not quite flat because of the time-dependent properties of the on-line filter. For the data taken in 1993, the filter was set for three timing loops in the ARC algorithm (see Sec. VII A) and caused a loss of efficiency beginning near +2 ns. This effect was noticeably reduced for the balance of the data. The background PDF for $\cos(\theta_{e\gamma})$ was a

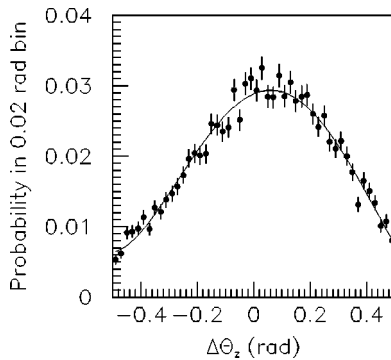


FIG. 22. A representative background PDF for $\Delta\theta_z$ generated by examining events out of time coincidence.

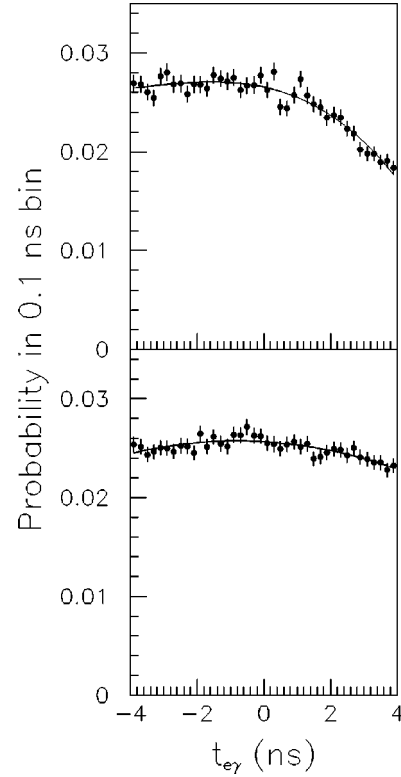


FIG. 23. The accidental-background PDF for the relative time between the positron and photon for 1993 (1994–1995) is shown in the upper (lower) panel. The smooth curve through the data was used in the likelihood analysis.

constant for all target intersection angles. The PDFs for E_e were obtained by normalizing the fits to the muon-decay spectrum, examples of which are shown in Figs. 8 and 20.

In Eq. (2), Q was taken from MC simulation of the IB and had correlations among the variables E_γ , E_e , and $\theta_{e\gamma}$. The PDFs for $t_{e\gamma}$ and $\Delta\theta_z$ were statistically independent and were obtained in an analogous way to P , except that the response was for a lower mean energy photon. The correlated matrix element varied by more than three orders of magnitude over the range of the likelihood function. If calculated by randomly sampling events over the entire range of the likelihood function, there would have been no statistics at the highest energies. Hence, it was calculated by convoluting the MC simulation of the IB process with the detector acceptance in small regions of the parameter space and weighting the passing events by the integrated IB matrix element for that region. The regions and branching ratios are given in Table VI. The overall PDF was normalized to unity.

The likelihood function evaluated the statistical separation between signal, IB, and background. Figure 24 shows the value of P/R for the data sample and for a set of MC events. The data largely had values below one but had a tail that extended out to around 300. The signal was peaked near one but had most of its area at values greater than 300. The values ran up to near 12,000 but are plotted only to 5000. The interpretation of the overlap of the two plots is that the measurement is not free of background.

To observe the impact of quality constraints in the pattern

TABLE VI. The branching ratios for the bins of the simulation of the correlated IB matrix element. All kinematically allowed $\theta_{e\gamma}$ are encompassed. The energies are in MeV.

E_γ	E_e			
	49-50	50-51	51-52	52-53
53.0	2.84^{-11}	1.22^{-11}	3.58^{-12}	3.36^{-13}
50.5	1.76^{-10}	8.02^{-11}	2.49^{-11}	2.44^{-12}
48.0	4.74^{-10}	2.21^{-10}	7.07^{-11}	7.01^{-12}
45.5	9.65^{-10}	4.53^{-10}	1.46^{-10}	1.46^{-11}
43.0				

recognition, they were relaxed to produce a sample 3 times larger. One event emerged with a large value of P/R that was significantly separated from the distribution. The value of P/R for this event was 3888, which made it resemble signal. Its kinematic properties were $E_\gamma = 52.58$ MeV, $E_e = 53.37$ MeV, $t_{e\gamma} = 0.028$ ns, $\Delta\theta_z = 0.068$ rad, and $\cos(\theta_{e\gamma}) = -0.99988$. In addition, it was within 19° of being perpendicular to the target and had 11 of 19 possible triples plus the outgoing Snow White anode as part of the positron track. The positron energy was located in the region of the spectrum that was particularly sensitive to the signal because the PDF for signal fell more slowly than the one for background. However, this event had a large positron $\chi^2_\nu = 4.90/(\text{degree of freedom})$, indicative of a ghost track. Therefore, the event was considered either unphysical or statistically insignificant, though if it were real, it would correspond to a branching ratio at the single event sensitivity of the experiment, $(2.3 \pm 0.2) \times 10^{-12}$. The adopted constraints produced a sample with considerably less background. The result presented below was stable against changes in the constraints; e.g., the higher value of $N_{e\gamma}$ was compensated by a corresponding increase in acceptance.

A plot of the two dimensional likelihood function is shown in Fig. 25. The contours of constant likelihood have their extrema along the $N_{e\gamma}$ and N_{IB} axes, demonstrating the

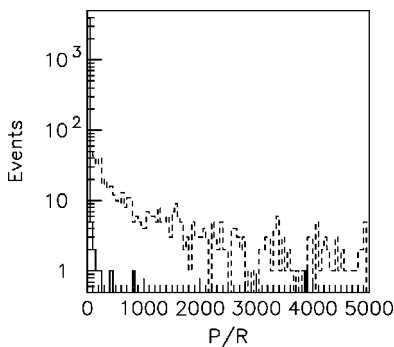


FIG. 24. The P/R distributions for the data (solid line) from this experiment and for the MC predicted signal (dashed line) for this experiment. The two hatched events were added to the data sample when the cuts were relaxed as discussed in the text.

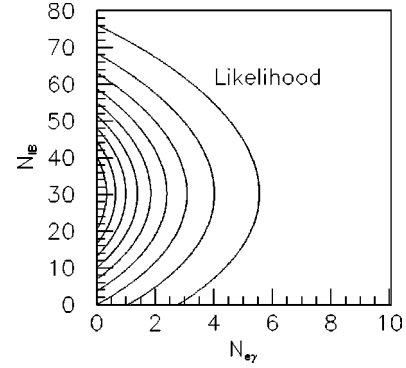


FIG. 25. A contour plot of the two-dimensional likelihood function as a function of the numbers of prompt events of IB and $\mu \rightarrow e\gamma$.

statistical independence of the separation between these two processes. The peak of the likelihood function was at $N_{e\gamma} = 0$ and $N_{IB} = 30 \pm 8 \pm 15$. The systematic error assigned to N_{IB} was due to the uncertainty in the shape of the background time spectrum when the events were filtered by the on-line program. The expected number of IB events was $36 \pm 3 \pm 10$, where the systematic error was due to finite resolution effects across the cut boundaries. The 90% confidence limit is the value for $N_{e\gamma}$ where 90% of the area of the likelihood curve lies below $N_{e\gamma}$ and N_{IB} is maximal. This value was $N_{e\gamma} < 5.1$. Therefore, the limit on the branching ratio is

$$\frac{\Gamma(\mu^+ \rightarrow e^+ \gamma)}{\Gamma(\mu^+ \rightarrow e^+ \nu \bar{\nu})} \leq \frac{5.1}{N_\mu} = 1.2 \times 10^{-11} (90\% \text{ C.L.}). \quad (7)$$

X. GOALS VS ACHIEVEMENTS

The 90%-confidence sensitivity for $\mu^+ \rightarrow e^+ \gamma$ for this experiment analyzed with the likelihood method is given by

$$S = \frac{N_{e\gamma}}{\left(\frac{\Omega}{4\pi}\right) \epsilon_e \epsilon_\gamma N_s}, \quad (8)$$

where the terms in the denominator are the fractional solid angle, the detection efficiency for each particle, and the total number of muon decays. The product of the first three terms in the denominator, neglecting correlations, is roughly the acceptance of the apparatus. These factors identify the major contributions to the acceptance and are given in the second column of Table VII. The product has the value 3.9×10^{-3} and can be compared to the $0.8 \times 4.3 \times 10^{-3} = 3.4 \times 10^{-3}$ given in Sec. IX B.

The sensitivity at which one event of background [27] should be seen is

$$\mathcal{B} = \left(\frac{R_\mu}{d} \Delta t\right) \left(\frac{\Delta E_e}{m_\mu/2}\right) \left(\frac{\Delta E_\gamma}{15m_\mu/2}\right)^2 \left(\frac{\Delta\theta}{2}\right)^2 f(\theta_\gamma) \eta_{IB\nu}. \quad (9)$$

The terms are the muon stop rate divided by the beam duty factor multiplied by the detector time resolution, the positron

TABLE VII. The contributions to the signal sensitivity of the MEGA experiment at the design stage and after a complete analysis of the data.

Quantity	Designed	Achieved	Degradation factor
$N_{e\gamma}$ (90% C.L.)	≤ 2.3	≤ 5.1	2.2
$\Omega/4\pi$	0.42	0.31	1.4
ϵ_e	0.95	0.53	1.8
ϵ_γ	0.051	0.024	2.1
N_s	3.6×10^{14}	1.2×10^{14}	3.0
Total factor			34.9

energy resolution in reduced units, the photon energy resolution in reduced units, the angular resolution, and the background reduction factors from photon angle traceback and inner bremsstrahlung veto. All resolutions are FWHM. The quadratic dependence of the photon energy term is related to the bremsstrahlung nature of the energy spectrum, while that of the angular resolution arises from phase space considerations.

The proposal for the MEGA experiment [28] predicted a 90%-confidence sensitivity for $\mu \rightarrow e\gamma$ as 9×10^{-14} . Later engineering considerations reduced this to 4×10^{-13} , primarily because (1) the solenoid could accommodate only three photon spectrometers instead of five, (2) each photon spectrometer had only two rather than three lead converter sheets (photon conversions in the innermost third sheet reconstructed poorly), and (3) the achievable overall solid angle was 30% smaller than proposed. Operation of the apparatus revealed a dramatically lower positron reconstruction efficiency and a somewhat lower photon reconstruction efficiency than expected. These were attributed to electronic cross talk among the anode and cathode readout channels of the positron spectrometer and among the photon spectrometer delay line cathodes.

The proposed sensitivity was essentially free of background. However, MC simulations performed after the detector was constructed showed degradations in the resolutions to a background free sensitivity of 1.6×10^{-12} . These losses were largely due to inadequacies of the early-stage simulations, where measurements of the responses of prototype detectors were not available. In particular, the scintillator time resolution was affected by the small number of photoelectrons emitted from the cathodes of the photomultiplier tubes, the photon energy resolution was affected by the use of delay lines rather than stereo cathodes, and the positron momentum resolution was degraded by changes in the geometry and wire configuration of the positron spectrometer. The single largest loss of background rejection capability came from the failure of the IBV detectors to perform as expected. As noted in Sec. III G, the IBV scintillators that were to line the upstream pole tip penetration were never installed. However, the downstream IBV detectors alone were expected to veto 40% of the photons above 51 MeV originating from $\mu \rightarrow e\gamma\nu\bar{\nu}$. But analysis of the IBV data demonstrated that only 3.5% of the high energy photons detected by the pair

TABLE VIII. The contributions to the background sensitivity of the MEGA experiment at the design stage and after a complete analysis of the data.

Quantity	Designed	Achieved	Degradation factor
R_μ (MHz)	30.0	15.0	0.5
$t_{e\gamma}$ (ns)	0.8	1.6	2.0
E_e (MeV)	0.25	0.54	1.5
E_γ (MeV)	1.7	1.7,3.0	1.6
$\theta_{e\gamma}$ (deg)	1.0	1.9	3.6
θ_γ (deg)	10.0	10.0	1.0
η_{IBV}	0.2	1.0	5.0
Total factor			43.3

spectrometers were associated with IBV hits, including 2% real and 1.5% random coincidences. This rate was essentially independent of photon energy for $E_\gamma > 42$ MeV, rather than increasing with increasing E_γ . For these reasons, the inner bremsstrahlung veto was not used in the final analysis.

The changes in sensitivity and resolution between design and final data analysis are given in Tables VII and VIII, respectively. In Table VIII, the degradation factor includes the appropriate power from Eq. (9). The photon energy resolution degradation factor is weighted by the fraction of events where the photon converted in the inner or outer lead sheet. In both tables, the total factor is the product of the individual factors.

The degradation factors in Tables VII and VIII arose principally from three phenomena: First, electronic cross talk in the positron spectrometer limited the muon stop rate, reduced the reconstruction efficiency, and degraded the energy and angular resolutions of the reconstructed tracks. Second, cross talk in the photon spectrometer delay line cathodes reduced the photon reconstruction efficiency and degraded the energy and conversion point resolutions. Finally, an accident in 1993, where the photon spectrometer was dropped from a crane at a height of about 30 cm, led to eventual crazing of the scintillators and a subsequent reduction of light output; this loss of light reduced the scintillator efficiency and worsened the positron-photon timing resolution.

XI. CONCLUSION

A high-precision search for the rare muon decay mode $\mu^+ \rightarrow e^+ \gamma$ has been performed with the MEGA detector. A maximum-likelihood analysis of the data established a new upper limit for the branching ratio of $\mathcal{B}(\mu^+ \rightarrow e^+ \gamma) < 1.2 \times 10^{-11}$ with 90% confidence. This upper limit constrains the existence of physics outside the standard $SU(3) \times SU(2) \times U(1)$ model of the strong and electroweak interactions, since $\mu \rightarrow e\gamma$ is predicted to occur in virtually all extensions that have been proposed. For example, in grand unified supersymmetric theories [3], this upper limit increases the lower limit on the masses of the mediating particles by 40%, relative to the lower limit that existed before the results of this experiment were first announced. Similarly,

if the recently reported, apparent deviation of the muon anomalous magnetic moment from the standard model prediction [2] is due to supersymmetry, this upper limit on the branching ratio for $\mu \rightarrow e \gamma$ sets stringent limits on the flavor-violating masses that occur in the minimal supersymmetric standard model [29].

ACKNOWLEDGMENTS

We are grateful for the support received from many LAMPF staff members and, in particular, P. Barnes, G. Garvey, L. Rosen and D. H. White. We wish gratefully to acknowledge the contributions to the construction and operation of the experiment from the engineering and technical staffs and undergraduate students at the participating institutions. The experiment was supported in part by the U.S. Department of Energy and the National Science Foundation.

APPENDIX A: PHOTON PATTERN RECOGNITION

The photon pattern recognition algorithms were optimized to find pair conversions due to high energy photons. Initially, active adjacent cells within the same drift chamber cylinder were combined into clusters of hits. If delay line information was available, contiguous drift chamber hits that had z values differing by more than 4 cm were assigned to separate clusters. Pattern recognition then began by classifying the edges of the events. To be considered as a candidate event, at least one member of the conversion pair had to pass through all three photon drift chambers in a pair spectrometer during its initial arc. Shower edges that appeared consistent with this hypothesis were identified as “3-side” edges. The other member of the pair was required to pass through at least the innermost and middle drift chambers, but not necessarily the outermost. Shower edges that appeared to arise from tracks that passed through only the inner two drift chambers of a pair spectrometer were identified as “2-side” edges. Typical events with 3-side and 2-side edges are shown in Fig. 26. The 3-side edges were allowed to have a maximum cluster width of two drift chamber cells in the first and second drift chambers to minimize ambiguities due to multiple passes. These constraints eliminated some high energy photon conversions, but they reduced background and improved resolution without significantly reducing the reconstruction efficiency. Events with satisfactory edges were then checked for possible vertices. For events with a 2-side edge, the vertex location was found by starting from the 2-side edge and locating the first set of hits in the outermost drift chamber. Connecting this with hits in the inner two drift chambers defined the candidate vertex location. Both minimum and maximum width constraints were imposed on the distance between the 2-side edge and the vertex. If the width constraints were not satisfied, the cells on the 2-side were considered to be noise hits and an attempt was made to reclassify the edge of the event as a 3-side edge.

The on-line pattern recognition algorithm allowed for multiple vertex candidates for events that were tagged as having 3-sides on both edges. Candidate vertex locations required more than one hit in the outermost drift chamber. This

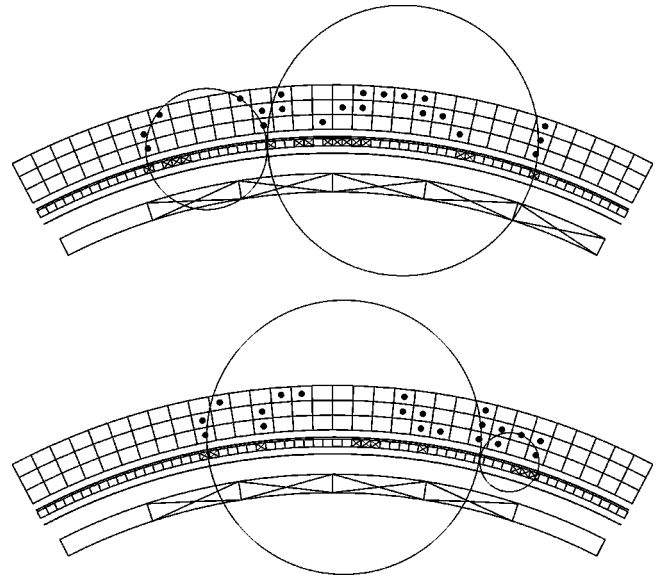


FIG. 26. End view of two typical photon spectrometer events. The detector elements, from inner to outer radius, are plastic scintillators, lead, MWPC, lead and three layers of drift chamber. Hits in plastic scintillator and MWPC cells are shown with an “ \times ” and hits in drift chamber cells are shown as solid circles. In the top event, both edges are classified as 3-side. The bottom event left edge corresponds to a 3-side and the right edge is a 2-side. The circles shown in the figures were fits from the photon spectrometer analysis code.

constraint eliminated most high energy Compton scattered photons with very little loss of efficiency for 52.8 MeV pairs. (This constraint was relaxed during the $\pi^0 \rightarrow \gamma\gamma$ studies described in Sec. VIII E for certain classes of electromagnetic showers induced by the higher energy photon.) A maximum of two contiguous cells was allowed in the innermost drift chamber for a vertex candidate associated with two 3-side edges. MC simulation was used to set additional restrictions for vertex candidates that involved non-contiguous cells in the middle and/or the outermost drift chambers.

The pair recognition algorithm was performed in the on-line analysis and then repeated during off-line processing. In the on-line code, a crude determination of the energy was made by estimating the transverse momentum from the width of the event and the longitudinal momentum using the difference in the vertex and edge z locations, coupled with the vertex to edge transverse distances. The photon conversion location, $(R_\gamma, \phi_\gamma, z_\gamma)$, was obtained from the vertex location and the time of conversion, T_γ , was obtained from scintillators that were hit below the edge cells.

In the off-line code, events were further processed by algorithms that determined those cells that were most likely associated with the initial arc of the conversion pair. The tagging process was repeated for each vertex candidate in an event. Tagged cells formed the set of drift chamber hits used in the circle fits for the events. A non-linear least-squares fitting routine was used to obtain the best circle fits for the conversion pair. The χ^2 that was minimized summed $(d_{meas} - d_{calc})^2 / \sigma_d^2$ over the tagged cells as well as $(v_{e^+} - v_{e^-})^2 / \sigma_v^2$, where d was the drift distance of each hit cell

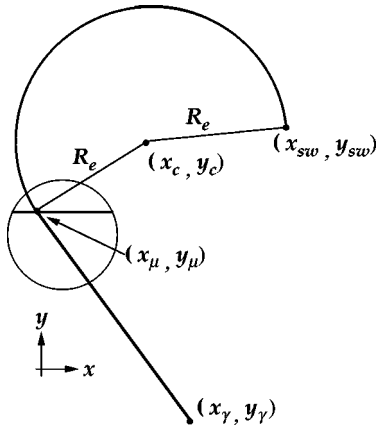


FIG. 29. This view along the axis of the positron helix leads to a determination of the center of the helical orbit and the x coordinate of the muon decay obtained from Eqs. (B5), (B6) and (B7).

The planar target sloped in the y - z plane, allowing y_μ to be determined from z_μ . Using Fig. 29, the coordinates of the axis of the helical orbit (x_c, y_c) and the x coordinate of the muon decay in the muon stopping target (x_μ) were calculated from the following three equations:

$$-\frac{y_\gamma - y_\mu}{x_\gamma - x_\mu} = \frac{x_\mu - x_c}{y_\mu - y_c}, \quad (\text{B5})$$

$$(x_{sw} - x_c)^2 + (y_{sw} - y_c)^2 = R_e^2, \quad (\text{B6})$$

$$(x_\mu - x_c)^2 + (y_\mu - y_c)^2 = R_e^2. \quad (\text{B7})$$

With (x_μ, y_μ, z_μ) determined, the value for r_γ was calculated. The entire process was repeated using these values to obtain better estimates of t_γ , t_e , x_μ , y_μ , z_μ , R_e , x_c , and y_c .

Employing the coordinates of the beginning (x_μ, y_μ, z_μ) , ending (x_{sw}, y_{sw}, z_{sw}) , and axis (x_c, y_c) of the helical positron orbit, the helix rotation angle $(\theta_{e\mu})$ was calculated from (x_μ, y_μ) to (x_{sw}, y_{sw}) . The total angle traversed by the positron can be written as

$$\theta_{e\mu} + 2\pi n_{loop} = \left(\frac{qBt_e}{m} \right), \quad (\text{B8})$$

where m is the mass of the positron and n_{loop} is the number of loops. The nearest integer value for n_{loop} was determined from Eq. (B8) and the integer result was substituted back in Eq. (B8) to obtain a better estimate of t_e . The new value of t_e was used in Eq. (B1) to improve the orbit parameters further. With the orbit parameters known, the spatial coordinates where the orbit intersected the positron MWPCs were calculated.

APPENDIX C: POSITRON PATTERN RECOGNITION

The principal job of the positron pattern recognition code was to find the space points, called clusters, where positrons crossed the MWPCs and then map the clusters into helical tracks. Clusters were defined as nearly contiguous groups of

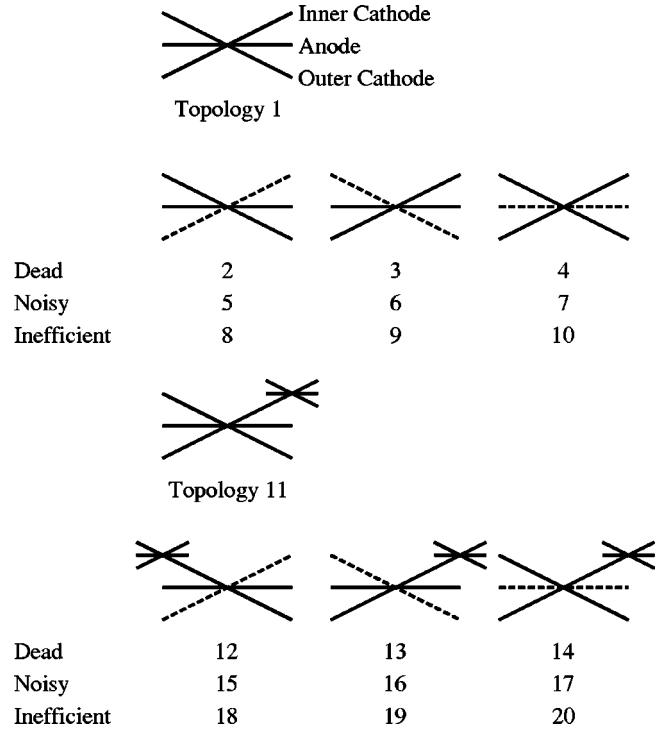


FIG. 30. The different types of space point topologies. The solid lines represent clean hits. Illustrations with dashed lines represent three distinct topologies, where the dashed line may be replaced by a dead channel, a noisy cluster, or a known inefficiency. They were assigned distinct numbers and were studied separately during the development of the pattern recognition program. Additional topologies were also defined and studied, such as triples with two noisy clusters, but were not used in the final analysis.

hits in either the anodes or cathodes that were normally associated with the response of a chamber to a track crossing. The clustering algorithm took into consideration the imperfections of the detector (about 7% dead wires and cathode stripes and inefficiencies in the chambers), as well as the dependence of cluster widths on the entry angle of the track with the chamber. The anodes and cathodes were treated slightly differently because of the differences in their modes of signal generation. Track reconstruction efficiency was mostly insensitive to the choice of clustering algorithm, but the method that was selected optimized the resolutions; the projection to the decay point in the target was more sensitive than the energy. For high rate data, clustering was only applied to chambers that were potentially involved in a signal event.

The term “double” describes the spatial overlap of an anode cluster with a cluster from one of the foils. A triple required the z coordinate of two doubles associated with a single anode be the same to within 1 cm. If a cathode cluster contributed to more than one double, only the two triples with the smallest differences in anode crossings were retained. Anode-only clusters were allowed in the Snow White chamber when positron tracks were leaving the chamber toward larger radial distance. Triples and doubles were of varying quality and were denoted according to their “crossing topologies.” The types of crossing topologies are displayed in Fig. 30. Noisy clusters had an excessive number of wires;

e.g., for the anodes, a noisy cluster in a dwarf contained more than 8 wires. Clusters in regions of known inefficiencies were noted. Clusters that could have been associated with another crossing were tagged, since it was possible for triples and doubles to be formed from random hits at high rates.

The high rate code only examined crossing topologies if the anode cluster was within the end-view ARC windows. Only crossing topologies 1, 2–7, and 11 were used as parts of tracks. The coordinates of the intersections were calculated from the centers of the cluster crossings. In the case of differing widths for inner and outer cathode clusters, the narrower width was used to determine the coordinate.

The intrinsic resolutions for a normal crossing were 0.065 cm rms for the anodes and 0.29 cm rms for the cathodes. The weights ($1/\sigma^2$) for fitting were assigned to the space points to reflect an intrinsic resolution, the entrance angle, and the differences in the cathode cluster widths. These weights, as a function of entrance angle and cluster widths, were in good agreement with the residuals from track fitting.

As an initial step in obtaining tracks, all combinations of three clean (e.g., <8 wires) anode-wire clusters were used to extract the parameters of circles that passed through these anodes. For high rate data, the combinations were restricted to groups of three clean anodes in distinct ARC windows. All wires (ignoring ARC windows) in the involved chambers were examined for anodes within a chord length of 0.75 cm, and successes were associated with this circle. The circle parameters were extracted by fitting these data. After all possible combinations were fit, the parameters were compared to eliminate duplicates.

There could be considerable ambiguity with respect to the number of loops a real track made for a given circle due to inefficiencies and accidental degeneracies of the hits. At high rates, the large number of hits resulted in many possibilities, some of which were artificial. Starting with circles, helical track fragments were sought by looking for straight lines in the unrolled system. Combinations of track fragments were compared to determine if they fell on the same straight line where the 2π ambiguity around the circle was considered. If enough fragments lie on the same straight line for a particular set of slopes and intercepts, a trial track was identified.

The trial track was then extended in both directions toward the target and toward the scintillators. If the extensions passed sufficiently close to triples having the correct topologies, these hits were added to the trial tracks. On the target side, there was an ambiguity as to the origin of the track, so

a minimum criterion for the number of triples and doubles in the first loop was applied. On the scintillator side, a final triple in the Snow White chamber was required for a track to be retained. Roughly, for a candidate track to be kept, it must retain 60%–70% of the possible hits.

Non-uniformities in the magnetic field led to a complexity in the above procedure for events with a high number of loops. Tracks still projected as circles but they deviated from a straight line in the unrolled view [30]. In order to keep these tracks, the extrapolation of the fragment slopes had to account for the deviations that increased the longitudinal distance traversed per loop as the field weakened. The field non-uniformities were small and well described by a polynomial; the ratio of the first and second terms to the 0^{th} term were $-1.8 \times 10^{-4} \text{ cm}^{-1}$ and $-7.1 \times 10^{-6} \text{ cm}^{-2}$, respectively, over the range of ± 70 cm. Though the terms were small, the corrections were many centimeters for an event making many loops.

Once the hits were identified, the parameters characterizing the track, the circumference around the chamber and the longitudinal position including the z -correction term, were extracted via a non-linear least squares fit. The circumference was chosen because the hits were confined to lie on the circles that were defined by the chamber wires. The parameters were defined by the helix equations

$$\begin{aligned} x(\phi) &= x_c + \rho \cos(\phi + \phi_0), \\ y(\phi) &= y_c + \rho \sin(\phi + \phi_0), \\ z(\phi) &= z_0 + (\rho \tan \lambda) \phi. \end{aligned} \quad (\text{C1})$$

The derivatives of the predicted measurements with respect to the parameters that were needed to make up the curvature matrix of the least squares fit are analytic, making the fitting process reasonably fast [23].

However, using this procedure it was possible to find the same track many times and, at high rates, to find false tracks. A number of criteria were used to sort the best candidates from the list to maximize the probability of finding only real tracks once. For multiple tracks associated with the same circle, the track with the greatest fractional occupancy was retained, and tracks with the same slope and center were concatenated to a single track. Tracks were required to have a certain minimum number of triples and doubles and the cutoffs depended on the number of loops and the number of dwarfs involved.

[1] Q.R. Ahmad *et al.*, Phys. Rev. Lett. **87**, 071301 (2001).
 [2] Muon $g-2$ Collaboration, H.N. Brown *et al.*, Phys. Rev. Lett. **86**, 2227 (2001).
 [3] R. Barbieri, L. Hall, and A. Strumia, Nucl. Phys. **B455**, 219 (1995); N. Arkani-Hamed, H.-C. Cheng, and L. Hall, Phys. Rev. D **53**, 413 (1996).
 [4] Y. Kuno and Y. Okada, Rev. Mod. Phys. **73**, 151 (2001).
 [5] R.D. Bolton *et al.*, Phys. Rev. D **38**, 2077 (1988).

[6] M.L. Brooks *et al.*, Phys. Rev. Lett. **83**, 1521 (1999).
 [7] P.A. Thompson *et al.*, Nucl. Instrum. Methods **161**, 394 (1979).
 [8] H.W. Reist *et al.*, Nucl. Instrum. Methods **153**, 61 (1978).
 [9] D. Aston *et al.*, “The LASS Spectrometer,” SLAC Technical Report No. 0298 1987.
 [10] D. D. Koetke *et al.* (in preparation).
 [11] M.D. Cooper *et al.*, Nucl. Instrum. Methods Phys. Res. A **417**,

- 24 (1998).
- [12] V. Armijo *et al.*, Nucl. Instrum. Methods Phys. Res. A **303**, 298 (1991).
- [13] LeCroy Corporation, 700 Chestnut Ridge Road, Chestnut Ridge, NY 10977-6499.
- [14] National Instruments Corporation, 6504 Bridge Point Parkway, Austin, TX 78730-5039.
- [15] Phillips Scientific Inc., 150 Hilltop Road, Ramsey, NJ 07446.
- [16] M. Barakat *et al.*, Nucl. Instrum. Methods Phys. Res. A **349**, 118 (1994).
- [17] C.A. Gagliardi *et al.*, Nucl. Instrum. Methods Phys. Res. A **273**, 117 (1988).
- [18] Y.K. Chen *et al.*, Nucl. Instrum. Methods Phys. Res. A **372**, 195 (1996).
- [19] R. Barber *et al.*, Nucl. Instrum. Methods Phys. Res. A **479**, 591 (2002).
- [20] W. R. Nelson, H. Hirayama, and D. W. O. Rogers, "The EGS4 Code System," SLAC Report No. 265, 1985.
- [21] "GEANT Detector Description and Simulation Tool," CERN Program Library Long Writeup W5013, 1993.
- [22] R. Talman, Nucl. Instrum. Methods **159**, 189 (1979).
- [23] K. M. Stantz, Ph. D. thesis, University of Indiana, 1997.
- [24] W. T. Eadie, D. Dryard, F. E. James, M. Roos, and B. Sadoulet, *Statistical Methods in Experimental Physics* (North-Holland, Amsterdam, 1971).
- [25] R. Bock *et al.*, Comput. Phys. Commun. **45**, 181 (1987).
- [26] W.W. Kinnison *et al.*, Phys. Rev. D **25**, 2846 (1982).
- [27] R. Engfer and H.K. Walter, Annu. Rev. Nucl. Part. Sci. **36**, 327 (1986).
- [28] LAMPF experiment 969, M. D. Cooper spokesperson.
- [29] Z. Chacko and G.D. Kribs, Phys. Rev. D **64**, 075015 (2001).
- [30] J. D. Jackson, *Classical Electrodynamics*, 2nd ed. (Wiley, New York, 1975).